ELSEVIER

Chemical Geology 186 (2002) 151–181

CHEMICAL GEOLOGY
INCLUDING
ISOTOPE GEOSCIENCE

www.elsevier.com/locate/chemgeo

The effect of melt composition on trace element partitioning: an experimental investigation of the activity coefficients of FeO, NiO, CoO, MoO_2 and MoO_3 in silicate melts

Hugh St.C. O'Neill*, Stephen M. Eggins

Research School of Earth Sciences, Australian National University, Canberra 0200, ACT, Australia

Received 29 May 2001; accepted 26 November 2001

Abstract

The thermodynamic theory describing the partitioning of trace elements between crystals and silicate melt implies that partition coefficients should depend on the major-element composition of the melt from two different causes, namely (1) the activity coefficient of the trace-element oxide component in the melt, and (2) the activities of all the major-element components needed to balance the trace-element substitution in the crystal (the "stoichiometric control"). Partition coefficients are also expected to vary with the composition of the crystal, and temperature and pressure. Because these variables cannot be controlled independently in direct crystal/melt partitioning studies, it has not been possible to disentangle their effects, or to determine their relative importance. In order to explore the effects of melt composition on activity coefficients of trace-element oxide components, the activity coefficients of five such components, MoO_2, MoO_3, FeO, NiO and CoO, were measured in 18 different melt compositions in the system $CaO–MgO–Al_2O_3–SiO_2$ plus one composition in $CaO–MgO–Al_2O_3–SiO_2–TiO_2$ at 1400 °C, by equilibration with the metal under controlled oxygen fugacity. MoO_2 and MoO_3 are expected to have geochemical properties similar to the High Field Strength Elements (HFSEs). The activity coefficients of MoO_2 and MoO_3 vary by factors of 20 and 60, respectively, over the range of compositions investigated. Their variation is highly correlated, and mainly depends on the amount of CaO in the melt, suggesting the influence of $CaMoO_3$ and $CaMoO_4$ complexes. The analogy between Mo and HFSEs implies that melt composition can be expected to have an important influence on HFSE partition coefficients. The activity coefficients of FeO, NiO and CoO vary by a factor of two over the same range of melt compositions, but show no simple dependence on any particular major-element oxide component. However, the activity coefficients of all three components are very highly correlated with each other. This means that the effect of melt composition can be largely eliminated if the ratios of two activity coefficients are taken, as, for example, when two-element distribution coefficients are used.

Keywords: Partition coefficients; Silicate melts; Thermodynamics; Mo; Fe; Ni; Co

1. Introduction

In the study of igneous rocks, trace element concentrations have long been used to constrain factors in their petrogenesis such as source enrichment, the style

* Corresponding author. Tel.: +61-2-6125-5159; fax: +61-2-6125-5989.

E-mail address: hugh.oneill@anu.edu.au (H.St.C. O'Neill).

0009-2541/02/$ - see front matter
PII: S0009-2541(01)00414-4

of melting (e.g., batch or fractional), the degree of melting, and the nature and extent of any subsequent fractional crystallization. Well-known equations exist relating the concentrations of a trace element M in melt and residue to the crystal/melt partition coefficients, $D_{\mathrm{M}}^{\mathrm{melt/crystal}}$, and the degree of melting, F, both for batch melting and fractional melting (e.g., Gast, 1968; Wood and Fraser, 1977). Increasingly, mathematical models for more complicated scenarios are being developed (e.g., DePaolo, 1981; Navon and Stolper, 1987; Spiegelman and Elliott, 1993; Richardson and McKenzie, 1994; O'Hara, 1995; Shaw, 2000). In all this modelling, the assumption has been made that values of $D_{\mathrm{M}}^{\mathrm{melt/crystal}}$ can be treated as constants. The same assumption has also made in Rare Earth Element (REE) inversion modelling (McKenzie and O'Nions, 1991). To what extent this assumption is reasonable, or whether it is wishful thinking, is difficult to judge, for there has been little in the way of empirical evidence as to how values of $D_{\mathrm{M}}^{\mathrm{melt/crystal}}$ might vary.

The factors causing values of $D_{\mathrm{M}}^{\mathrm{melt/crystal}}$ to vary can be appreciated if the thermodynamic theory describing crystal-melt equilibrium is used to provide the conceptual framework. The initial step is to describe the partitioning reaction using a balanced chemical reaction between thermodynamically valid components (Banno and Matsui, 1973). Such a reaction can be written generally as:

$$\mathrm{MO}_{x/2}\cdot\sum_{\mathrm{Z}} n_{\mathrm{crystal}}\ \mathrm{ZO}_{y/2} = \mathrm{MO}_{x/2}{}_{\mathrm{melt}} + \sum_{\mathrm{Z}} n_{\mathrm{melt}}\ \mathrm{ZO}_{y/2} \quad (1)$$

where $\mathrm{MO}_{x/2}$ is the oxide component of M in the silicate melt, x is the valence state of M, and $\mathrm{ZO}_{y/2}$ are the major-element oxide components (such as SiO_2, $AlO_{1.5}$, etc.) that are needed to make up the component $\mathrm{MO}_{x/2}\cdot\sum_{\mathrm{Z}} n\ \mathrm{ZO}_{y/2}$, which has the appropriate stoichiometry necessary to substitute into the crystal. Hence, at equilibrium:

$$\ln\left(a_{\mathrm{MO}_{x/2}}^{\mathrm{melt}}\Big/ a_{\mathrm{MO}_{x/2}\cdot\sum_{\mathrm{Z}} n\ \mathrm{ZO}_{y/2}}^{\mathrm{crystal}}\right) = -\Delta_{\mathrm{m}}G^{\mathrm{o}}/RT - \sum_{\mathrm{Z}} n\ \ln a_{\mathrm{ZO}_{y/2}}^{\mathrm{melt}} \quad (2)$$

where $\Delta_{\mathrm{m}}G^{\mathrm{o}}$ is the fictive free energy of melting of pure $\mathrm{MO}_{x/2}\cdot\sum_{\mathrm{Z}} n\ \mathrm{ZO}_{y/2}$ relative to the sum of its pure liquid oxide components (i.e., its actual free energy of melting less the free energy of mixing of the liquid oxide components). This convention permits the activity of a component in the melt ($a_{\mathrm{MO}_{x/2}}^{\mathrm{melt}}$) to be defined conveniently with respect to a standard state of pure liquid $\mathrm{MO}_{x/2}$ at the temperature and pressure of interest. The activity of the trace-element component in the crystal $\left(a_{\mathrm{MO}_{x/2}\cdot\sum_{\mathrm{Z}} n\ \mathrm{ZO}_{y/2}}^{\mathrm{crystal}}\right)$ is similarly defined with respect to pure solid $\mathrm{MO}_{x/2}\cdot\sum_{\mathrm{Z}} n\ \mathrm{ZO}_{y/2}$ (which may be a hypothetical substance) at the temperature and pressure of interest. Activities are then related to concentrations in the usual way, through the use of activity coefficients:

$$a_{\mathrm{MO}_{x/2}}^{\mathrm{melt}} = X_{\mathrm{MO}_{x/2}}^{\mathrm{melt}}\cdot\gamma_{\mathrm{MO}_{x/2}}^{\mathrm{melt}} \quad (3)$$

$$a_{\mathrm{MO}_{x/2}\cdot\sum_{\mathrm{Z}} n\ \mathrm{ZO}_{y/2}}^{\mathrm{crystal}} = X_{\mathrm{MO}_{x/2}\cdot\sum_{\mathrm{Z}} n\ \mathrm{ZO}_{y/2}}^{\mathrm{crystal}}\cdot\gamma_{\mathrm{MO}_{x/2}\cdot\sum_{\mathrm{Z}} n\ \mathrm{ZO}_{y/2}}^{\mathrm{crystal}} \quad (4)$$

The partition coefficient is defined as:

$$D_{\mathrm{M}}^{\mathrm{melt/crystal}} = k\cdot X_{\mathrm{MO}_{x/2}}^{\mathrm{melt}}/X_{\mathrm{MO}_{x/2}\cdot\sum_{\mathrm{Z}} n\ \mathrm{ZO}_{y/2}}^{\mathrm{crystal}} \quad (5)$$

where k is a constant to convert from mole fractions to the more customarily used concentrations by weight. Therefore:

$$\ln D_{\mathrm{M}}^{\mathrm{melt/crystal}} = -\Delta_{\mathrm{r}}G^{\mathrm{o}}/RT - \sum_{\mathrm{Z}} n\ \ln a_{\mathrm{ZO}_{y/2}}^{\mathrm{melt}} - \ln\gamma_{\mathrm{MO}_{x/2}}^{\mathrm{melt}} + \ln\gamma_{\mathrm{MO}_{x/2}\cdot\sum_{\mathrm{Z}} n\ \mathrm{ZO}_{y/2}}^{\mathrm{crystal}} + \ln k \quad (6)$$

It is evident that values of $D_{\mathrm{M}}^{\mathrm{melt/crystal}}$ should depend on:

(1) T (and probably P). The terms on the RHS of Eq. (6) can be divided up into enthalpy and entropy terms, where the entropy terms (mainly the entropy of melting) are likely to be small relative to enthalpy terms (particularly those associated with activity coefficients). Hence, to a first approximation, $\ln D_{\mathrm{M}}^{\mathrm{melt/crystal}} = \Delta h/RT$, where Δh represents these enthalpy terms. Thus, $\mathrm{d}(\ln D_{\mathrm{M}}^{\mathrm{melt/crystal}})/\mathrm{d}T = \Delta h/R$. The

importance of this approximation is that it indicates that the change of $D_M^{melt/crystal}$ with temperature is related to its magnitude, tending towards unity at infinite temperature. Igneous processes generally operate over a restricted range of inverse temperature, so that temperature is not likely to have much of a *direct* effect on trace-element partition coefficients. An anomalously large change of $D_M^{melt/crystal}$ with temperature (or pressure) is likely to be a secondary effect of the other factors listed below.

(2) The major-element composition of the crystal, through $\gamma_{MO_{x/2}} \cdot \sum_Z n \cdot ZO_{y/2}^{crystal}$.

(3) The major-element composition of the melt, through two quite distinct factors:

a) $\sum_Z n \cdot \ln a_{ZO_{y/2}}$, the activities of the major-element components in the melt required by crystal stoichiometry. Here, we call these the "structural components". Takahashi and Irvine (1981) have also referred to this as the "stoichiometric control".
b) $\gamma_{MO_{x/2}}^{melt}$, the activity coefficient of the oxide component of M in the silicate melt.

The question of which of these variables are of practical importance has been much debated in the literature. Recently, the importance of the composition of the crystalline phase has been the subject of a vigorous burst of attention due to the development of lattice strain theory (e.g., Blundy and Wood, 1991, 1994). Other authors, however, continue to promote the role of silicate melt composition as a key variable (e.g., Nielsen, 1988; Kohn and Schofield, 1994).

The main reason why this important issue remains controversial is that, in direct studies of crystal/melt partitioning, it is difficult to vary independently melt composition, crystal composition, temperature or pressure, so as to disentangle the effects of each of these variables. This is simply but unavoidably because crystals of a given composition are only in equilibrium with a very limited range of melt compositions, for any given temperature and pressure. The range over which temperature and pressure can be varied while still maintaining equilibrium between melt and crystals is of course also very limited. Apparent changes of $D_M^{melt/crystal}$ with temperature or pressure may be due to the changing major-element composition of the crystal or the melt. Moreover, it is usually not possible to disentangle the two kinds of effects that melt composition may have.

However, from thermodynamic modelling of phase equilibria, there is now a fair amount of independent evidence on how the activities of the major-element components that comprise the $\sum_Z n \cdot \ln a_{ZO_{y/2}}$ term may vary; but little is known for any trace element on how $\gamma_{MO_{x/2}}^{melt}$ may depend on melt composition. This is particularly true for incompatible trace elements, although it is these elements that are of interest in much of trace-element modelling.

For elements whose oxide components are easily reduced to the metal (i.e., siderophile elements), it is possible to construct experiments that measure the effect of melt composition on $\gamma_{MO_{x/2}}^{melt}$ directly, while keeping all the other relevant variables constant. This is done by measuring the oxygen fugacity of the oxidation–reduction reaction:

$$\underset{metal}{M} + x/4\ O_2 = \underset{silicate\ melt}{MO_{x/2}} \tag{7}$$

Hence, at equilibrium:

$$\ln \gamma_{MO_{x/2}}^{sil\ melt} = \frac{-\Delta_f G^o_{(MO_{x/2})}}{RT} - \ln X_{MO_{x/2}}^{sil\ melt} + \frac{x}{4} \ln fO_2 + \ln a_M^{metal} \tag{8}$$

If the metal M is pure, $\ln a_M^{metal} = 0$, while $\Delta_f G^o_{(MO_{x/2})}$ is a constant at constant T and P. Hence, the activity coefficient is directly related to the metal's apparent solubility (given by $X_{MO_{x/2}}^{sil\ melt}$), if fO_2 is known. The method works because the solubility of elements in their zero valence (i.e., metallic) state in silicate melts is negligibly small, hence only the oxidized components $MO_{x/2}$ are present. By varying oxygen fugacity, this may be verified and also the valence state x determined. Many elements occur in more than one valence state in silicate melts, but this too can be resolved since for appropriate elements fO_2 can be varied experimentally over several orders of magnitude.

Recent results of this type of experiment for the trace element Ni, which dissolves in silicate melts as the divalent cation Ni^{2+} (hence the oxide component NiO) have suggested that the compositional dependence of $\gamma_{NiO}^{sil\ melt}$ is small (e.g., Holzheid et al., 1997;

Ertel et al., 1997). However, earlier studies generally reported significant compositional dependence (Campbell et al., 1979; Dudson and Fraser, 1981; Pretorius and Muan, 1992). Ni^{2+} behaves geochemically like the major-element cations Mg and Fe^{2+}, for which it substitutes readily in most crystalline phases. Its behaviour in silicate melts might therefore be anticipated to follow the behaviour of Mg and Fe^{2+}, an idea that has been explored in the model of Doyle (e.g., Doyle and Naldrett, 1987).

But what about other trace elements that have chemical properties unlike any of the major elements in silicate melts? As examples, consider the so-called "High Field Strength Elements" (HFSEs). These are elements with high formal valence and relatively small ionic radii, such as the refractory lithophile elements Zr, Hf, Nb, and Ta. Perhaps U and Th, which are of particular interest in trace-element studies because of U-series disequilibrium modelling, and have high valence albeit somewhat larger ionic radii, could be included in this group. All these elements are now almost routinely determined in a trace element analysis of an igneous rock. The siderophile element Mo, which is less routinely determined, also has high formal valence and smallish ionic radius in both its common oxidation states, Mo^{4+} and Mo^{6+}, and is known empirically to behave like the HFSE Nb during mantle melting (Fitton, 1995). Thus, Mo of either valency could also be classified as a HFSE. This element lends itself well to study via equilibrium (1), as shown by Holzheid et al. (1994). However, Holzheid et al. (1994) investigated only one silicate melt composition, namely the diopside–anorthite eutectic composition in the simple system $CaO–MgO–Al_2O_3–SiO_2$. Walter and Thibault (1995) then reported that the metal/silicate melt partition coefficients of Mo (and also W) increase dramatically (by more than two orders of magnitude) at constant T, P and fO_2 as the composition of the silicate melt was changed from basaltic to komatiitic. If this were correct, it would imply that a modest amount of olivine fractionation could change a melt composition sufficiently to have an enormous effect on the partition coefficients of any elements with similar sensitivity to melt composition (i.e., HFSEs and U and Th, perhaps). In turn, this might put in doubt all inferences from U-disequilibrium series modelling, for example.

Here, we report an investigation of the effects of melt composition on the solubility of Mo in a wide variety of silicate melts in the systems $CaO–Al_2O_3–SiO_2$, $MgO–Al_2O_3–SiO_2$, and $CaO–MgO–Al_2O_3–SiO_2$ plus one composition in the quinary $CaO–MgO–Al_2O_3–SiO_2–TiO_2$ with 20 wt.% TiO_2). In order to facilitate comparison with the compatible elements Fe, Ni and Co, we also investigated the solubilities of these elements in the same melts. Since two oxidation states of Mo (Mo^{4+} and Mo^{6+}) occur in silicate melts in the range of oxygen fugacity that is accessible in these type of experiments (Holzheid et al., 1994), we have studied the effect of melt composition on both oxidation states. Effectively, we therefore obtain data on two HFSE analogues (i.e., Mo^{4+} and Mo^{6+}).

The partitioning of Fe, Ni, Co and Mo between the silicates of the Earth's mantle and the Earth's metallic core is potentially useful in constraining models for the accretion and primary differentiation of the Earth (e.g., O'Neill and Palme, 1998). Obviously, metal/silicate-melt partition coefficients may also be sensitive to silicate melt composition, and recently Righter and Drake (1997) have suggested a simple parameterization for this compositional dependence. The present data should be useful in testing their suggestion, and also addressing the general question of whether activity coefficients of trace elements in silicate melts can be usefully approximated by this kind of generalized approach.

For elements M that are solid metals at the chosen experimental temperature, a simple experimental method can be used to study their solubility in silicate melts according to reaction (7). A drop of the silicate melt is suspended from a wire loop of M in a conventional muffle furnace, under a suitable gas mixture to control oxygen fugacity (e.g., Holzheid et al., 1994, 1997). This tried and proven experimental technique has been used here.

1.1. Silicate melt compositions

Nineteen silicate melt compositions were studied, four in the ternary CAS, two in the ternary MAS, 12 in the quaternary CMAS, and one in the system $CMAS–TiO_2$. Compositions were selected so as to be liquid at our chosen experimental temperature of 1400 °C. This criterion limits the composition space

available in the ternary CAS and MAS systems to small areas near eutectics; compositions were chosen using the phase diagrams (Figs. 630 and 712 in Levin et al., 1964). For the CMAS system, compositions were selected using two complimentary approaches. In one approach, six low-melting-point (eutectic or peritectic) compositions were chosen, guided by the work of Longhi (1987). In the other approach, compositions are based on the anorthite–diopside eutectic composition (42% An, 58% Di, by weight, previously studied by Holzheid et al., 1994), to which were added the maximum amounts of the four components SiO_2, Mg_2SiO_4, $MgSiO_3$ and $CaSiO_3$ soluble in this composition at 1400 °C. The CMAS compositions covered thus include some near their liquidus as well as some that are as far below the liquidus as it is possible to go in this simple system. The composition in the CMAS–TiO_2 system was obtained by adding 20% TiO_2 to the An–Di eutectic.

In order to achieve maximum accuracy in this study, we did not attempt to investigate melt compositions containing other siderophile-element components, notably FeO, an important component in natural silicate magmas. The reason for this is that activity-composition relations in alloys often show large and complex deviations from ideality, potentially causing the uncertainties attendant in calculating a_M^{metal} to obscure the effects in $\gamma_{MO_{x/2}}^{sil\ melt}$. Nor can compositions containing volatile elements such as Na or K be investigated easily using the present experimental method since these elements would be lost by volatilization during the experiments because of the low fO_2s involved.

2. Experimental

2.1. Sample equilibration

Compositions were prepared from reagent grade MgO, Al_2O_3 and TiO_2, all dried before weighing at 1100 °C, fine-grained SiO_2 prepared from $SiO_2{\cdot}nH_2O$ ("silicic acid") by dehydrating at 1100 °C, and $CaCO_3$, dried at ~ 300 °C. Mixtures were homogenized by grinding under acetone in an agate mortar, pressed into pellets and decarbonated by heating slowly to ~ 1100 °C, followed by regrinding.

Samples were equilibrated using the wire-loop method in a conventional vertical tube furnace equipped for gas mixing, using $CO–CO_2$ mixtures to control fO_2. To prepare the loops, powdered melt compositions were rendered into a slurry using polyethylene oxide. Loops made from pure metal in the form of wire or strips cut from foil were dipped into the slurry, which was then allowed to dry. The loop plus its load of dried slurry were then, one at a time, lowered into a furnace at 1400 °C under flowing Ar–H_2 mixture, to melt the composition and drive off any remaining polyethylene oxide. If needs be, the process was repeated until enough sample adhered to the loop.

Six or seven wire loops of different silicate melt composition were suspended from a circular cage made from 0.5 mm Pt wire, braided double for strength, attached to a small alumina ring. We call this arrangement a "chandelier". The "chandelier" was hung by its alumina ring onto a hook, bent into the end of a strong 0.5 mm diameter Pt–Rh wire recycled from an ancient furnace. The Pt–Rh wire had been threaded through one bore of an 8 mm OD four-bore alumina tube, two other bores of which housed the wires for a type B Pt–Rh thermocouple. The samples were loaded into the tube furnace at 600 °C. This temperature is sufficiently low that if the loops swing into each other or onto the wall of the furnace tube, they do not stick. The appropriate $CO–CO_2$ gas mixture is then turned on, and the furnace heated to 1400 °C at 6 °C/min. Samples are drop-quenched by opening the furnace at the bottom and pulling the Pt–Rh wire from which the "chandelier" is suspended, which straightens the hook, causing the "chandelier" to drop into a beaker of water. Quoted run times are taken from when the furnace reaches 1400 °C to the time of quenching.

Occasionally, some samples fall prematurely, stick together, or stick to the side of the furnace during quenching. Such failures explain some of the apparent gaps in the data.

The composition of the $CO–CO_2$ gas mixture was set using Tylan FC2800 mass flow controllers. For this study, all experiments were done using the same two mass flow controllers; that for CO had a maximum flow rate of 400 SCCM (standard cubic centimeters per minute), that for CO_2 20 SCCM. Gas flows from the controllers were checked from time to time using a bubble flow meter. Agreement between nom-

inal and measured flow rates was within 2% within most of the range of the mass flow controllers. The operation of the controllers was further tested three times during the series of experiments reported here, by means of a $SIRO_2$ yttria-stabilized zirconia oxygen sensor, with flowing air as the reference electrode. The performance of zirconia-based oxygen sensors degrades noticeably at 1400 °C after only a few hours in the low fO_2 regime of the present experiments, and hence the oxygen sensor was not used during the actual equilibration experiments. The tests with the YSZ sensor were carried out at 1120 °C, with no samples in the furnace. For gas mixtures between 20% and 90% CO, the difference between log fO_2 as measured by the sensor and that calculated from the gas mix was 0.05 ± 0.01, the sensor systematically recording the more oxidizing conditions. There are numerous factors that can affect both ways of measuring fO_2, and it is not possible to decide unequivocally which method is more likely to be correct. We have chosen to report fO_2 as calculated from the gas mix, without further correction. We assume that the nonsystematic error (i.e., between different runs) is expected to be about ± 0.02 log fO_2, based on experience. Any systematic error is not included in the statistical analysis of the results. The gas flow was fed into the furnace at the bottom and exited from the top, whence it bubbled through a small oil trap. A constant bubble rate through the oil trap is a sensitive check that there are no leaks in the furnace (e.g., from a cracked muffle tube). Mo solubility was studied as a function of fO_2 from $10^{-11.63}$ to $10^{-9.6}$ bars (corresponding to gas mixtures from 97% to 75.8% CO), while Fe, Ni and Co solubilities were studied at one fO_2 condition each. For Ni and Co, the fO_2 conditions of $10^{-9.60}$ and $10^{-11.63}$ bars, respectively, were selected to give optimum amounts of Ni and Co dissolved in the melt, which, from analytical and theoretical considerations, is about 2000–3000 ppm. The Fe experiments were conducted at fO_2 of $10^{-12.61}$ bars (99% CO), which is approximately the lowest fO_2 achievable in the Fe–C–O system in equilibrium with pure Fe metal, since carbon starts to dissolve significantly into Fe metal at lower fO_2, inducing melting. Because of the extreme CO/CO_2 ratio, the absolute accuracy of this fO_2 must be lower than for the other experiments, although we are satisfied from replicate experiments that the mass flow controllers still give good precision even at this ratio. However, precision would also be expected to drop off were an even more extreme ratio used. The Fe experiments contain about 3 wt.% Fe in the melt. For comparison, the Fe–"FeO", Co–CoO, Ni–NiO and Mo–MoO_2 solid state univariant equilibria lie at $10^{-9.71}$, $10^{-7.23}$, $10^{-5.77}$ and $10^{-9.23}$ bars, respectively, at 1400 °C (O'Neill and Pownceby, 1993; O'Neill, 1986).

Temperatures were controlled to ± 1 °C, using a type B thermocouple external to the furnace tube, and were measured using a second type B thermocouple, held in the alumina tube from which the "chandelier" is suspended. Type B thermocouples show a slight drift at the lowest fO_2s of the experiments reported here, presumably due to poisoning by carbon. The drift was typically ~ 1 °C/day, and is thus observable, but not experimentally significant in the present context. All runs are believed to be within ± 2 °C of the nominal temperature of 1400 °C.

After the quench, the loops with their attached beads of silicate glass were unhooked from the "chandelier", mounted in 1-in. epoxy discs, and polished for analysis by electron microprobe and laser-ablation ICP-MS.

2.2. Analytical methods

The major element compositions of all samples were checked by electron microprobe analysis, using a CAMECA Camebax in the EDS mode. Standardization and ZAF correction procedures are described in Ware (1981). Ni, Co and Mo metal wires were used as the standards for these elements, and the calibration for Fe was also checked against Fe wire. Operating conditions were 15 kV and 6 nA. Mean compositions of all samples are given in Table 1. When compositions are normalized to 100% in the CMAS system (i.e., ignoring the amount of the dissolved siderophile element), there is no evidence for statistically significant changes in composition between samples run at different fO_2s. The most likely change in composition would be some loss of Si at the lowest fO_2, because of volatility of SiO(g), but there is no evidence of this.

Concentrations of Fe, Ni, Co and, in a few runs, Mo, were determined by electron microprobe analysis using WDS. The pure metals were used as standards. Counting times were 100 s on peak, 10 s on back-

Table 1
Major element compositions of silicate melts, from energy-dispersive electron microprobe analysis of the run products of the Mo, Ni and Co experiments, normalized to 100% and averaged

Melt	CaO	MgO	Al_2O_3	SiO_2	NBO/T	$(\sum N_{ZO_{y/2}}^{sil\ melt})^a$
AD6						
AD eutectic	24.1 (5)	10.6 (1)	15.2 (2)	50.1 (4)	0.960 (18)	1.824
AD + Fo (15%)	20.5 (3)	16.9 (3)	12.9 (2)	49.6 (2)	1.220 (18)	1.864
AD + En (60%)	15.2 (2)	20.6 (2)	9.3 (2)	54.8 (2)	1.262 (13)	1.878
AD + Wo (140%)	38.0 (4)	4.6 (1)	6.6 (2)	50.6 (2)	1.496 (17)	1.764
AD + Qz (50%)	16.2 (6)	6.9 (2)	10.0 (3)	66.8 (6)	0.553 (21)	1.768
AD + TiO_2 (25%)[b]	19.1 (3)	8.5 (1)	12.1 (1)	40.7 (2)	–	1.710
CMAS7						
A (1 bar eutectic, 1240)	16.4 (1)	11.9 (3)	15.3 (1)	56.3 (3)	0.707 (14)	1.825
B (fo + pr-en, 1371)	8.8 (1)	19.7 (5)	13.8 (2)	57.5 (4)	0.831 (23)	1.873
C (fo + o-en, 1353)	16.5 (1)	19.1 (5)	6.3 (1)	57.8 (3)	1.301 (25)	1.854
D (fo + sp, 1358)	12.7 (1)	17.9 (5)	21.0 (2)	48.2 (3)	0.765 (23)	1.885
E	21.6 (2)	18.7 (4)	9.7 (1)	49.7 (4)	1.482 (23)	1.867
F (SiO_2 + di, 1330)	18.6 (1)	13.3 (3)	5.6 (1)	62.3 (3)	1.058 (15)	1.808
G (an + di + wo + SiO_2, 1129)	25.8 (4)	2.4 (2)	12.3 (2)	59.4 (5)	0.649 (16)	1.750
CAS and MAS						
MAS1 (pr-en + cord + SiO_2, 1355)	–	20.2 (1)	17.2 (1)	62.6 (2)	0.482 (4)	1.879
MAS2 (fo + cord + sapph, 1370)	–	25.2 (2)	22.7 (2)	52.1 (2)	0.613 (8)	1.936
CAS1 (pswo + gehl + an, 1265)	39.0 (1)	–	18.9 (1)	41.9 (2)	0.955 (4)	1.765
CAS2 (pswo + gehl + rank, 1310)	47.4 (3)	–	11.3 (3)	41.2 (4)	1.619 (18)	1.754
CAS3 (an + mull + SiO_2, 1345)	10.7 (3)	–	19.0 (3)	70.3 (5)	0.006 (6)	1.733
CAS4 (an + wo + SiO_2, 1170)	33.8 (2)	–	12.3 (1)	53.8 (2)	0.848 (7)	1.740

Low-melting point melt compositions (i.e., eutectic or peritectic compositions) are identified by the phases crystallizing at, and the temperature of, the eutectic/peritectic.

[a] Number of moles of the major-element oxides in 100 g of melt.

[b] Plus 19.6 (3) wt.% TiO_2.

ground. Beam size was 2 μm. Counts were converted to concentrations using the ZAF correction procedure, with compositional factors determined from the EDS analyses. Results are reported as the mean and standard deviation of at least 10 spot analyses on each sample.

Concentrations of Mo, Ni and Co were also determined by laser-ablation ICP-MS, using an ArF (193 nm) excimer laser coupled to an Agilent 7500S quadrupole mass spectrometer via a custom-built ablation cell and aerosol transfer system. The spatial resolution and analytical capabilities of this instrumentation have been outlined elsewhere (Eggins et al., 1997, 1998), and have proved ideally suited for this study. In particular, the Mo metal nuggets present in many Mo samples present a problem that can only be overcome (or reduced to a tractable level) by sampling at high spatial resolution. To maximize the spatial resolution, we used a relatively small beam diameter (< 30 μm). It is also necessary to maximize instrument response times to enable analysis of nugget-free glass between encountering successive nuggets. This is achieved with an ablation cell design that incorporates a very small active volume (~ 1 cm^3), with the transfer of ablated materials directly to the ICP-MS torch via narrow bore (2 mm ID) FEP tubing. In the absence of a post-ablation signal smoothing device, a laser repetition rate of 20 pulses/s has been necessary to obtain a stable sample feed to the ICP-MS and to avoid laser sampling noise that otherwise would compromise analysis quality due to the sequential nature of ICP-MS analysis. To avoid inter-element fractionation effects arising from the preferential condensation of more refractory components during sampling from high aspect ratio ablation pits (≥ 1), samples were rastered in the plane of the focused

laser beam (30 μm/diameter) at ~ 0.5 mm/min. This enabled compositional profiling along precisely cut low-aspect ratio trenches (30 μm wide × ~ 10 μm deep). About 0.1–0.2 μm of material is removed from the sample by each laser pulse.

LA-ICP-MS data collection was performed by peak hopping (1 point/peak) employing 20 ms dwell times on selected isotopes of the bulk matrix glass (^{25}Mg, ^{27}Al, ^{29}Si, ^{43}Ca, ^{49}Ti) and of the metal of interest (^{59}Co or ^{60}Ni and ^{61}Ni or ^{95}Mo and ^{98}Mo). The instrument was calibrated using NIST610 (synthetic soda-lime glass comprising 70.0 wt.% SiO_2, 2.0 wt.% Al_2O_3, 11.45 wt.% CaO, 460 μg/g Mg, 437 μg/g Ti, 459 μg/g Ni, 400 μg/g Co, 440 μg/g Mo; Pearce et al., 1997, NIST certified values, and Sylvester and Eggins, 1997) as the primary reference material. USGS BCR2g glass was employed as a secondary reference material (54.6 wt.% SiO_2, 10.50 wt.% Al_2O_3, 6.95 wt.% CaO, 3.40 wt.% MgO, 2.35 wt.% TiO_2, 12.5 μg/g Ni, 15.5 μg/g Co, 262 μg/g Mo) to check data quality. Data reduction was performed following removal where present of anomalous time slices containing ablated metal nugget material by standard laser ablation ICP-MS procedures (see Longerich et al., 1996) using ^{43}Ca (or ^{29}Si in Ca-absent experiments) as an internal standard (derived from electron microprobe measurements).

The other major elements (i.e., Si, Al, Mg, and Ti) were also checked by laser ablation to confirm the

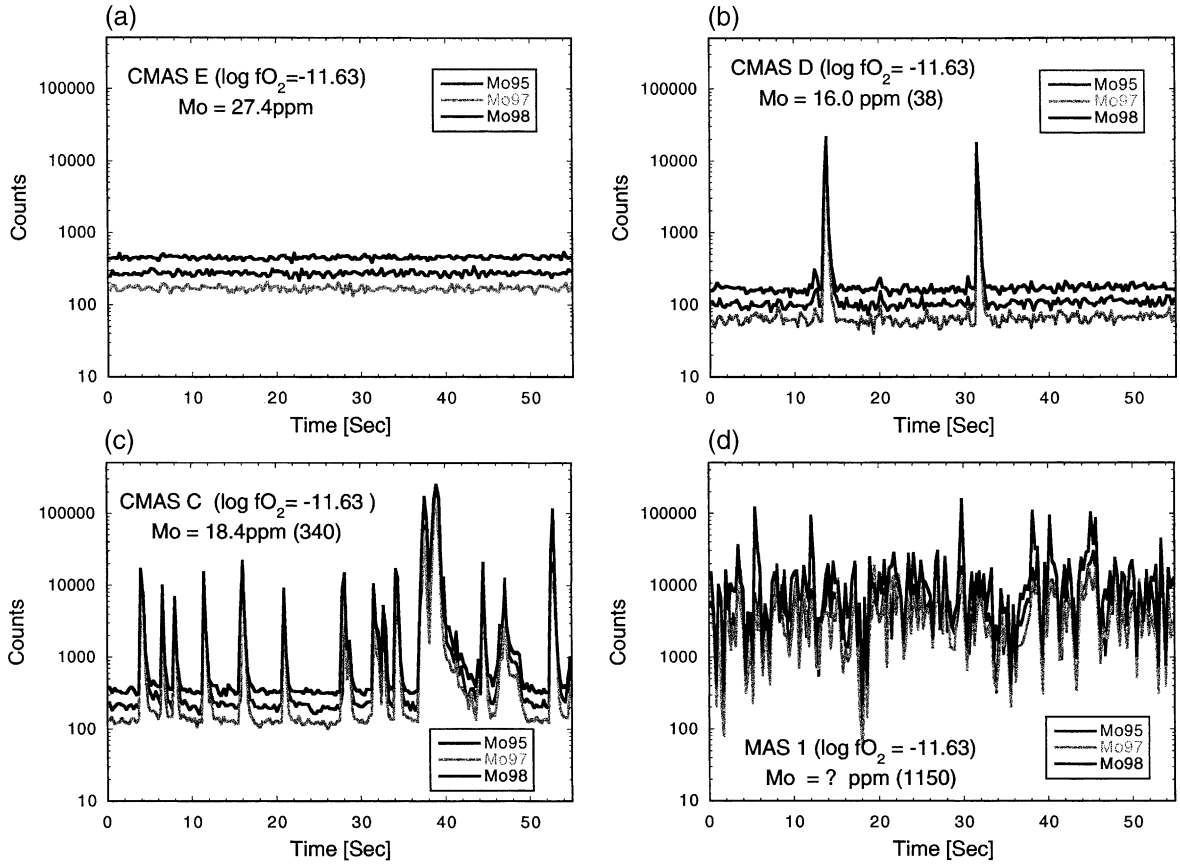

Fig. 1. Examples of ^{95}Mo, ^{97}Mo and ^{98}Mo time-resolved spectra for glasses containing differing Mo nugget number densities ranging from (a) completely homogeneous without nuggets, through (b) sporadic (~ 10^{6-7}/cm^3), to (c) common (~ 10^{7-8}/cm^3), and (d) overwhelmingly abundant nuggets (>10^8/cm^3). Note that observed count rate variation between nuggets is consistent with counting statistic variability. The resolution of glass Mo contents from nugget contributions is enabled by the rapid washout characteristics of the ANU laser ablation ICP-MS (i.e., >3 orders of magnitude intensity reduction in 2 s). A comparison of Mo concentrations calculated by excluding and including nuggets (latter in brackets) is given on each panel.

identity of each glass analysed. Virtually all analyses were performed in duplicate or triplicate, and the analytical reproducibility was typically better than 2–3% relative. Examples of spectra obtained in four samples representative of different levels of nugget contamination are illustrated in Fig. 1.

Many of the Mo samples contained nuggets of Mo metal. The maximum size of the nuggets is far greater than in stirred-crucible experiments on Highly Siderophile Element solubilities (Ertel et al., 1999, 2001), and in many samples, the nuggets are large enough to be visible with an optical microscope. The problem is most severe in compositions with high silica, hence high viscosity. In a few cases, the density of the nuggets was so great as to preclude analysis even using the microanalytical techniques of this study, and for the composition CAS3, the nugget problem was so severe that no Mo solubilities could be obtained at any fO_2. However, in most cases, the micronuggets could easily be identified by the LA-ICP-MS analytical method in time-resolved spectra, as shown in Fig. 1, and hence filtered out from reported results. We have interpreted occasional abnormally high spot analyses as also due to nuggets, and such analyses were not included in the reported results. Nuggets were not a problem in experiments with the other metals.

2.3. Equilibration times

The time needed to reach steady state Mo solubilities, which is necessary but alas not sufficient to prove or even to infer equilibrium because of the nugget problem (see Ertel et al., 2001), was investigated at one fO_2 ($10^{-10.60}$ bars) for one set of

Table 2
Results of Mo solubilities (in ppm) from LA-ICP-MS analysis

Melt	log fO_2/time									
AD6	−11.63	−11.27	−11.00	−10.80	−10.60	−10.60	−10.60	−10.20	−9.80	
	44 h	88.5 h	64.5 h	48 h	45 h	13.8 h	4 h	45.2 h	47.3 h	
AD	21.9	60.2		201	395	405	420	1329	4693	
AD+Fo	22.9	65.5	139	200	408	417	412	1486		
AD+En	17.4	50.0	99	148	286	306	304	991	3682	
AD+Wo	52.8	134	310	501		1007	1097	3602	14159	
AD+Qz	13.1	27.0	61.6	87.5	163		320	636	2042	
AD+TiO_2	35.6	92.0	184	269	492	503	508	1606	5350	
Melt	log fO_2/time									
CMAS7	−11.63	−11.27	−11.00	−10.80	−10.60	−10.40	−10.20	−10.00	−9.80	−9.60
	69 h	64 h	68 h	92 h	48 h	63 h	69 h	67 h	90 h	93 h
A	16.1	34.5	71	116	219	402	843	1377	2164	4657
B	13.9	33	61	101.5	188	382	724	1152	2063	3884
C	18.4	51	97	161	299	548	1203	1784	3547	6104
D	16.0	38	83	127	247	448	968	1605	2453	5582
E	27.4	71.5	162	246	495	925	2039	3484	5743	10608
F	19.0	45	87	150	277	515	1159	1826	3210	5490
Melt	log fO_2/time									
MAS and CAS	−11.63	−11.27	−11.00	−10.60	−10.20	−9.80				
	65 h	45 h	44 h	60 h	44.5 h	68 h				
MAS1				103	340	1134				
MAS2	12.4	27.2	52	148	440	1472				
CAS1	68.7		405	(1452)	4200	16665				
CAS2	171.5	507	1105	3550	12760	46020				
CAS3										
CAS4	33.8		185	559	1952	6892				

compositions by performing replicate experiments for 4, 13.8 and 45 h (Table 2). No systematic difference is detectable between the 13.8 and 45 h experiments, indicating that a steady state is reached in the shorter time, at least. The experiment at 4 h has slightly higher levels of Mo in the most silica-rich sample, although the steady state value is achieved in the others. However, the concentration of suspended particles of metallic Mo is higher in these short-duration samples. All other runs were of greater than 44 h duration. The metal-loop experiments of Holzheid et al. (1994, 1997) were of comparable duration (~ 50 h).

Analogous metal solubility experiments on several highly siderophile elements have repeatedly shown that the apparent steady state values sometimes may not correspond to true chemical equilibrium, due to the persistence of tiny particles of metal ("micro-nuggets") suspended in the melt (e.g., Ertel et al., 1999, 2001). To make the inference that equilibrium is attained also requires other factors to be considered, in particular, homogeneity on a suitable microanalytical scale, and the change of solubility with fO_2.

3. Results

3.1. Experimental results, accuracy and precision

Electron microprobe analyses of silicate melt major-element compositions are summarized in Table 1, in the form of the mean and standard deviations of analyses of all Mo, Ni and Co experiments, normalized to 100%. Mo solubilities are reported in Table 2, Ni and Co and solubilities in Table 3, and compositions of the Fe-bearing experiments in Table 4.

All the Ni and Co samples and 25 of the Mo samples with relatively high Mo concentrations (>1000 ppm) were also determined by electron microprobe analysis, and these results are compared with the LA-ICP-MS analyses in Fig. 2a–c. For the Mo samples, regression of the two data sets, weighted assuming an uncertainty of 3% for the LA-ICP-MS analyses and the observed standard deviations of the electron microprobe analyses, which are mostly in the range 1–4%, gives:

$$[\mathrm{Mo}]_{\mathrm{EMP}} = 0.985(\pm 0.009)\ [\mathrm{Mo}]_{\mathrm{LA-ICP-MS}}$$

Table 3
Co and Ni solubilities (in ppm)

Melt composition	Ni ($\log fO_2 = -9.60$)		Co ($\log fO_2 = -11.63$)	
	LA-ICP-MS	EMP	LA-ICP-MS	EMP
AD6	63 h		68 h	
AD eutectic	2038	1843 (69)	2804	3071 (88)
AD + Fo	1888	1801 (91)	2894	3143 (88)
AD + En	2272	2157 (56)	3696	3845 (86)
AD + Wo	2231	2270 (85)	3107	3522 (174)
AD + Qz	1675	1671 (90)	2831	2946 (75)
AD + TiO_2	2826	2700 (77)	4268	4246 (89)
CMAS7	92 h		69 + 17 h[a]	
A	2053	2021 (65)	3222	3228 (108)
B	2406	2358 (111)	3792	3557 (76)
C	2482	2472 (37)	3824	3842 (70)
D	2174	2055 (127)	2904	2880 (64)
E	1921	1759 (84)	2999	3093 (92)
F	2296	2261 (59)	3974	3679 (116)
G	1990	1928 (105)	3273	3165 (113)
CAS and MAS	68.5 h		65.5 h	
MAS1	2479	2503 (83)	4135	4004 (82)
MAS2	2701	2657 (48)	4218	4301 (197)
CAS1	1351	1317 (53)	1899	2017 (92)
CAS2	1367	1350 (64)	1947	2018 (86)
CAS3	1106	1018 (36)	2404	2272 (71)
CAS4	1876	1832 (50)	3208	3528 (160)

[a] The sample holder stuck at the attempted quench after 69 h. The samples were therefore removed from the top of the furnace, remounted and run for a further 17 h.

The reduced chi-squared (χ^2_v) for the regression is 1.84, indicating that the weighting of the data is realistic. Since the concentration of the NIST 610 standard is only known to ~ 5% (Pearce et al., 1997), the level of agreement is something of a fluke, but it does lend confidence to the absolute accuracy of the measurements.

A similar comparison between electron microprobe and LA-ICP-MS results for Ni and Co are shown in Fig. 2b,c. Regressions for these data give:

$$[\mathrm{Ni}]_{\mathrm{EMP}} = 0.970(\pm 0.010)\ [\mathrm{Ni}]_{\mathrm{LA-ICP-MS}} \quad \chi^2_v = 0.47$$

$$[\mathrm{Co}]_{\mathrm{EMP}} = 1.010(\pm 0.010)\ [\mathrm{Co}]_{\mathrm{LA-ICP-MS}} \quad \chi^2_v = 1.59$$

assuming an uncertainty of 3% in the LA-ICP-MS analyses.

Table 4
Compositions of silicate melts in equilibrium with metallic Fe at log $fO_2 = -12.61$, from EDS electron microprobe analysis

Melt composition	CaO	MgO	Al_2O_3	SiO_2	FeO	X_{FeO}
AD6 (44.5 h)						
AD eutectic	22.3	9.8	14.8	49.6	3.49 (3)	0.0269 (2)
AD + Fo	19.8	16.2	12.6	48.1	3.33 (6)	0.0251 (4)
AD + En	14.1	20.0	9.3	52.4	4.22 (3)	0.0315 (3)
AD + Wo	36.9	3.77	5.8	49.7	3.75 (2)	0.0299 (5)
AD + Qz	15.9	6.9	10.4	62.7	4.15 (7)	0.0328 (6)
AD + TiO_2	18.0	7.8	11.7	38.7	4.79 (9)[a]	0.0394 (7)
CMAS7 (68 h)						
A	15.3	11.7	15.1	54.3	3.53 (6)	0.0271 (4)
B	8.2	19.3	13.6	54.8	4.12 (9)	0.0308 (7)
C	15.3	18.7	6.3	55.3	4.47 (6)	0.0337 (4)
D	12.1	17.4	20.7	46.7	2.82 (16)	0.0210 (12)
E	20.2	18.2	9.9	48.3	3.39 (6)	0.0254 (4)
F	17.2	13.0	5.7	58.6	5.42 (5)	0.0420 (4)
G	24.4	2.2	11.8	57.3	4.22 (4)	0.0339 (3)
CAS and MAS (50 h)						
MAS1	–	19.3	17.2	58.7	4.76 (8)	0.0356 (6)
MAS2	–	24.0	22.4	48.7	4.81 (7)	0.0350 (5)
CAS1	36.8	–	18.7	42.0	2.49 (6)	0.0198 (4)
CAS2	45.3	–	11.1	41.0	2.53 (16)	0.0202 (12)
CAS3	10.4	–	19.6	67.9	2.02 (6)	0.0163 (4)
CAS4	31.5	–	12.0	52.6	3.91 (4)	0.0315 (4)

[a] Plus 19.0 wt.% TiO_2.

3.2. Mo^{4+} and Mo^{6+} solubilities and activity coefficients

The Mo solubilities for a representative composition (CMAS7-E) are plotted as a function of fO_2 in Fig. 3. The data do not plot on a straight line, but show distinct curvature in log [Mo] versus log fO_2 space, caused by a change in the oxidation state of Mo from Mo^{4+} at low fO_2 to Mo^{6+} at high fO_2. This change in valence state was previously observed by Holzheid et al. (1994), and occurs in all compositions, albeit over slightly different fO_2s.

For each composition, the Mo concentrations were converted to mole fractions according to the relationship:

$$(X^{\text{sil melt}}_{MoO_2} + X^{\text{sil melt}}_{MoO_3}) = \frac{[\text{Mo}] \times 10^{-4}/95.94}{[\text{Mo}] \times 10^{-4}/95.94 + \sum N^{\text{sil melt}}_{ZO_{y/2}}} \quad (9)$$

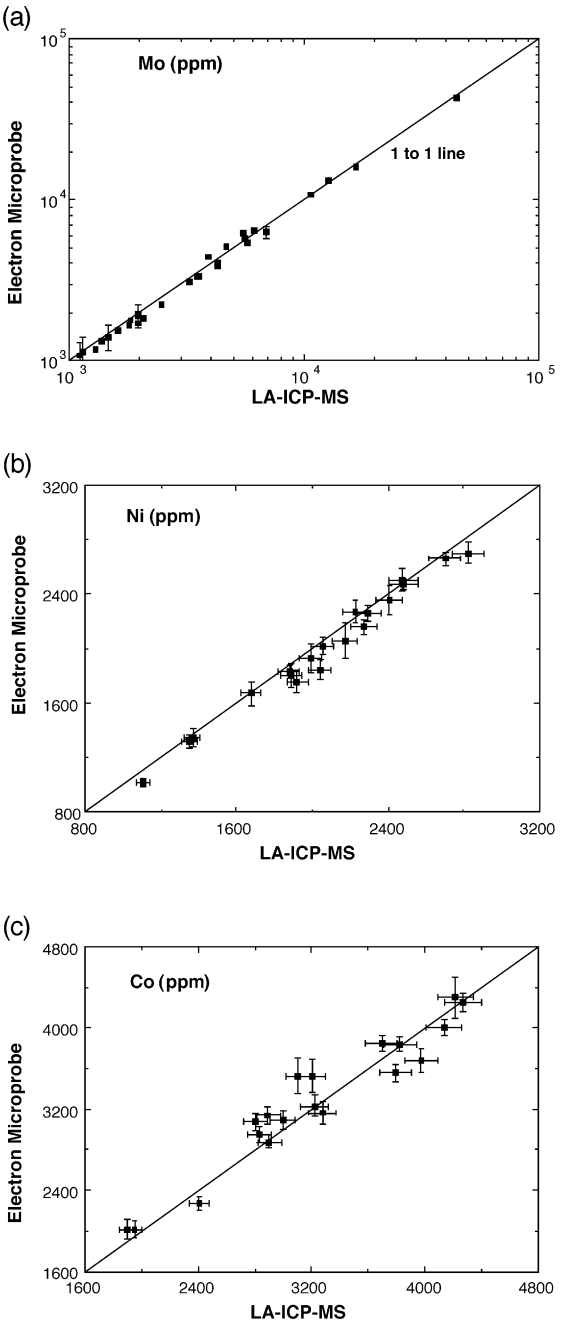

Fig. 2. Comparison between electron microprobe and laser-ablation ICP-MS analyses for (a) Mo (logarithmic scale), (b) Ni and (c) Co. Error bars are one standard deviation, assuming ± 3% for the LA-ICP-MS analyses.

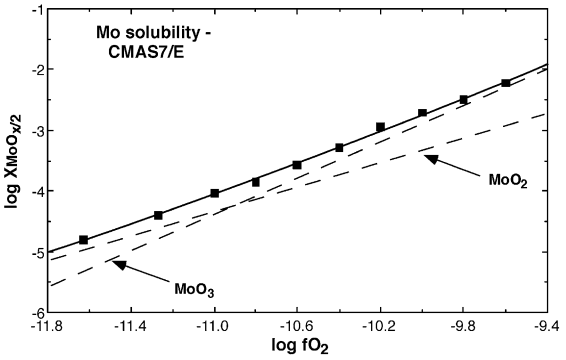

Fig. 3. Example of the solubility of Mo in one CMAS melt (CMAS7-E, see Table 1) at 1400 °C as a function of oxygen fugacity. One-standard deviation errors are about the size of the symbols. The best fit to the data from the regression analysis is shown as the smooth curve, with the calculated individual contributions from Mo^{4+} and Mo^{6+} given by the dashed lines.

where [Mo] is the concentration of Mo in ppm, 95.94 is the atomic weight of Mo, and $\sum N_{ZO_{y/2}}^{\text{sil melt}}$ is the total number of moles of the major-element oxides on a single cation basis (i.e., $N_{SiO_2}^{\text{sil melt}} + N_{AlO_{1.5}}^{\text{sil melt}} + N_{CaO}^{\text{sil melt}} + N_{MgO}^{\text{sil melt}}$) in 100 g of Mo-free melt. The values of $\sum N_{ZO_{y/2}}^{\text{sil melt}}$ for all melts are given in Table 1. They do not vary much.

The data for each melt composition were then fitted by nonlinear least squares regression to the equation:

$$(X_{MoO_2}^{\text{sil melt}} + X_{MoO_3}^{\text{sil melt}}) = Q^{MoO_2}(fO_2) + Q^{MoO_3}(fO_2)^{1.5} \quad (10)$$

using a weighting of ±3% for $(X_{MoO_2}^{\text{sil melt}} + X_{MoO_3}^{\text{sil melt}})$ and ±0.02 in log fO_2. The parameters $Q^{MoO_{x/2}}$ are solubility constants for each valence state, to be determined for each melt composition by the regression. Results are summarized in Table 5. During the fitting procedure, it was found that all the samples from one run, namely CMAS7 at log $fO_2 = -10.20$, plotted significantly off the curves established by the other nine runs for this set of compositions (e.g., see Fig. 3), indicating a systematic experimental error of about 0.06 in log fO_2 for this run. Such an error could arise, for example, if the auto-zeroing on the mass flow controllers failed to operate correctly. The samples from this run were eliminated from the regression analysis.

The individual solubilities of the MoO_2 and MoO_3 components (i.e., Mo^{4+} and Mo^{6+}, respectively) obtained from the regression analysis are shown in Fig. 3 for the representative composition CMAS7-E.

Activity coefficients may be calculated from the values of $Q^{MO_{x/2}}$ by combining Eqs. (1) and (3) to obtain:

$$\ln\gamma_{MoO_{x/2}}^{\text{sil melt}} = \frac{-\Delta_f G^o_{(T,1\ \text{bar})}(MoO_{x/2})}{RT} - \ln Q^{MO_{x/2}} \quad (11)$$

For comparison with the behaviour of other oxide components, it is helpful to define the standard state as the pure solid metal but pure liquid $MoO_{x/2}$, both at the temperature of interest. In general, if the pure solid were chosen as the standard state for the oxide component, the resulting activity coefficients would include the entropy of melting, and thus change greatly with temperature. This gives a misleading impression of the complexity of the thermodynamics (e.g., see discussion in Holzheid et al., 1997). For

Table 5
Results of nonlinear regression analysis of the Mo solubility data as a function of oxygen fugacity

Melt	Number of data	Q^{MoO_2} ($\times 10^{-6}$)	Q^{MoO_3} ($\times 10^{-11}$)	χ_ν^2
AD6				
AD eutectic	6	3.79 (34)	10.20 (84)	0.49
AD + Fo	6	3.94 (41)	10.64 (120)	1.93
AD + En	7	3.07 (25)	7.12 (62)	1.57
AD + Wo	7	7.56 (86)	32.86 (239)	0.83
AD + Qz	7	2.28 (16)	3.89 (38)	3.78
AD + TiO_2	7	7.74 (47)	9.50 (106)	1.02
CMAS7				
A	9	2.82 (17)	4.46 (33)	1.57
B	9	2.47 (14)	3.79 (28)	1.35
C	9	3.44 (22)	6.66 (46)	0.49
D	9	2.75 (18)	5.42 (37)	1.27
E	9	4.52 (35)	12.86 (78)	0.98
F	9	3.39 (21)	6.22 (44)	0.99
CAS and MAS				
MAS1	3	1.16 (31)	2.25 (40)	0.06
MAS2	6	2.34 (13)	1.88 (26)	1.14
CAS1	5	11.61 (126)	39.07 (309)	1.11
CAS2	6	27.67 (302)	114.21 (846)	0.25
CAS4	5	6.20 (58)	15.31 (133)	0.16

Uncertainties of 3% in Mo concentration and 0.02 in log fO_2 were assumed.

Table 6
Standard state free energy data used for calculating activity coefficients

Reaction	$\Delta_r G^o_{(T,\ 1\ bar)}$ (J mol^{-1})	References
$Mo(s)+1.5O_2=MoO_3(liq)$	$-725\,778+521.915T-41.5033T\cdot\ln T$	Chase (1998)
$Mo(s)+O_2=MoO_2(s)$	$-603\,268+337.460T-20.6892T\cdot\ln T$	O'Neill (1986)
$MoO_2(s)=MoO_2(liq)$	$(2200-T)\times 31.4$[a]	See discussion in text
$Fe(s)+0.5O_2=FeO(liq)$	$-244\,118+115.559T-8.474T\cdot\ln T$	O'Neill and Pownceby (1993), and Barin et al. (1989); see Holzheid et al. (1997)
$Ni(s)+0.5O_2=NiO(liq)$	$-185\,092+99.844T-4.898T\cdot\ln T$	
$Co(s)+0.5O_2=CoO(liq)$	$-187\,746+91.371T-5.672T\cdot\ln T$	

[a] From $\Delta_r G^o_{(T,\ 1\ bar)}=(T_m-T)\Delta_m S^o_{(T,\ 1\ bar)}$ with $T_m=2200$ K and $\Delta_m S^o_{(T,\ 1\ bar)}=31.4$ J K^{-1} mol^{-1}.

MoO_3, the thermodynamic data for the liquid standard state are well known, but MoO_2 decomposes (to Mo metal plus MoO_3 gas) before it melts, and nothing is known about its thermodynamic properties in the liquid state. Here, we have made a rough estimate based on a hypothetical melting point of 2200 K (similar to TiO_2) and an entropy of melting of 31.4 J K^{-1} mol^{-1}, as suggested by Chase (1998) for the entropy of melting of TiO_2. The adopted thermodynamic data and their sources are given in Table 6. Since only one temperature was investigated, the values of $\Delta_f G^o_{(T,\ 1\ bar)}$ (MoO_2) and $\Delta_f G^o_{(T,\ 1\ bar)}$ (MoO_3) are constants, and any errors in the adopted values has no bearing on the discussion that follows, which centres on relative changes in the activity coefficients with melt composition. Activity coefficients calculated from Eq. (11) are reported in Table 7.

There is evidently a large change in the solubilities, hence activity coefficients, of both Mo^{4+} and Mo^{6+} with silicate melt composition. In the CMAS system, values of Q_{MoO_2} and Q_{MoO_3}, hence $\gamma^{sil\ melt}_{MoO_2}$ and $\gamma^{sil\ melt}_{MoO_3}$, change by factors of three and nine, respectively (Table 4, see also Fig. 4). Include the MAS and CAS compositions and the range increases to well over an order of magnitude—a factor of 20 for Q_{MoO_2} and of 60 for Q_{MoO_3}.

There is an excellent correlation between $\gamma^{sil\ melt}_{MoO_2}$ and $\gamma^{sil\ melt}_{MoO_3}$ (Fig. 4). Intriguingly, the TiO_2-rich composition falls off this correlation line, due to an enhanced solubility of Mo^{4+} over Mo^{6+}. Leaving this composition out, regression of the remaining 16 data pairs gives:

$$\log \gamma^{sil\ melt}_{MoO_2} = 1.49(\pm 0.06)\log \gamma^{sil\ melt}_{MoO_3} - 3.59(\pm 0.14) \quad (12)$$

with $\chi^2_\nu=2.9$, using the uncertainties in Table 7. Much of the misfit is due to one composition, MAS2, with no CaO and relatively low levels of dissolved Mo. Without this composition, the value of χ^2_ν would be 1.6. Although the relationship between $\gamma^{sil\ melt}_{MoO_2}$ and $\gamma^{sil\ melt}_{MoO_3}$ is just an empirical one, the low value of χ^2_ν indicates that the uncertainties in activity coefficients

Table 7
Trace-element activity coefficients of MoO_2, MoO_3, FeO, NiO, and CoO in CMAS silicate melts at 1400 °C

Melt	γ_{MoO_2}	γ_{MoO_3}	γ_{FeO}	γ_{NiO}	γ_{CoO}
AD6					
AD eutectic	136 (12)	0.303 (25)	1.367 (11)	2.52 (6)	1.12 (3)
AD + Fo	131 (14)	0.290 (33)	1.468 (25)	2.70 (7)	1.11 (3)
AD + En	168 (13)	0.433 (38)	1.167 (10)	2.30 (5)	0.88 (2)
AD + Wo	68 (8)	0.094 (7)	1.231 (19)	2.12 (5)	0.98 (3)
AD + Qz	227 (16)	0.793 (78)	1.121 (19)	2.86 (7)	1.08 (3)
AD + TiO_2	67 (4)	0.325 (36)	0.935 (17)	1.44 (3)	0.61 (2)
CMAS7					
A	183 (11)	0.692 (51)	1.359 (22)	2.42 (5)	1.00 (3)
B	209 (12)	0.814 (61)	1.193 (27)	2.12 (5)	0.90 (2)
C	150 (10)	0.463 (32)	1.091 (14)	2.03 (3)	0.85 (2)
D	188 (12)	0.569 (39)	1.76 (10)	2.37 (7)	1.15 (3)
E	114 (9)	0.240 (15)	1.450 (24)	2.70 (7)	1.09 (3)
F	152 (10)	0.496 (35)	0.875 (9)	2.15 (4)	0.82 (2)
G	–	–	1.091 (14)	2.40 (6)	0.95 (3)
CAS and MAS					
MAS1	446 (117)	1.37 (24)	1.034 (17)	2.04 (5)	0.81 (2)
MAS2	221 (12)	1.64 (23)	1.052 (14)	1.94 (6)	0.81 (2)
CAS1	44 (5)	0.079 (6)	1.863 (45)	3.56 (9)	1.62 (4)
CAS2	19 (2)	0.027 (2)	1.82 (11)	3.48 (9)	1.58 (4)
CAS3	–	–	2.263 (59)	4.39 (11)	1.29 (2)
CAS4	83 (8)	0.201 (18)	1.168 (13)	2.54 (5)	0.94 (2)

Errors are one standard deviation and do not include systematic errors, e.g., in the standard state thermodynamic data.

(Table 7) are reasonable. This latter point is important when attempting to determine the factors controlling the values of $\gamma_{MoO_2}^{sil\ melt}$ and $\gamma_{MoO_3}^{sil\ melt}$ as a function of melt composition since it means that a satisfactory model must explain the data to the level of these uncertainties.

The main influence on the variation in $\gamma_{MoO_2}^{sil\ melt}$ and $\gamma_{MoO_3}^{sil\ melt}$ is the amount of CaO in the melt, as shown in Fig. 5a,b, where log $\gamma_{MoO_2}^{sil\ melt}$ and log $\gamma_{MoO_3}^{sil\ melt}$ are plotted against X_{CaO}. These plots also show that the anomaly in the TiO_2-rich composition is due to a lower value of $\gamma_{MoO_2}^{sil\ melt}$ rather than anything in the $\gamma_{MoO_3}^{sil\ melt}$ datum.

However, even omitting the TiO_2-rich composition, a simple model relating log $\gamma_{MoO_2}^{sil\ melt}$ and log $\gamma_{MoO_3}^{sil\ melt}$ to X_{CaO} is not sufficient to account for all the variation. For example, a linear relationship yields values of χ_v^2 of 9.7 and 11.3 for the MoO_2 and the MoO_3 data, respectively. Including a term in $(X_{CaO})^2$ brings down the value of χ_v^2 for the MoO_2 data to 3.9, but hardly affects the quality of the fit to the MoO_3 data. Nevertheless, it is clear that the functional form of the relationship between the activity coefficients and X_{CaO} needs to use the logarithm of the activity coefficients.

This logarithmic nature of the functional relationship suggests that a regular or subregular (Margules) type of solution model might be appropriate. The activity coefficient of a trace-element component (i.e., the activity coefficient of a component at infinite dilution) in the multicomponent subregular solution

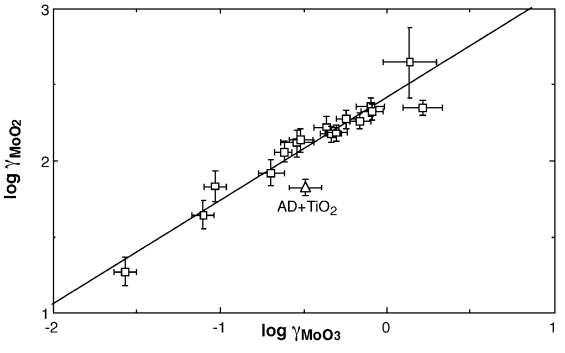

Fig. 4. Empirical correlation between $\gamma_{MoO_2}^{sil\ melt}$ and $\gamma_{MoO_3}^{sil\ melt}$. Error bars are one standard deviation. Note that the TiO_2-rich composition ($AD + TiO_2$) falls well off the best-fit line.

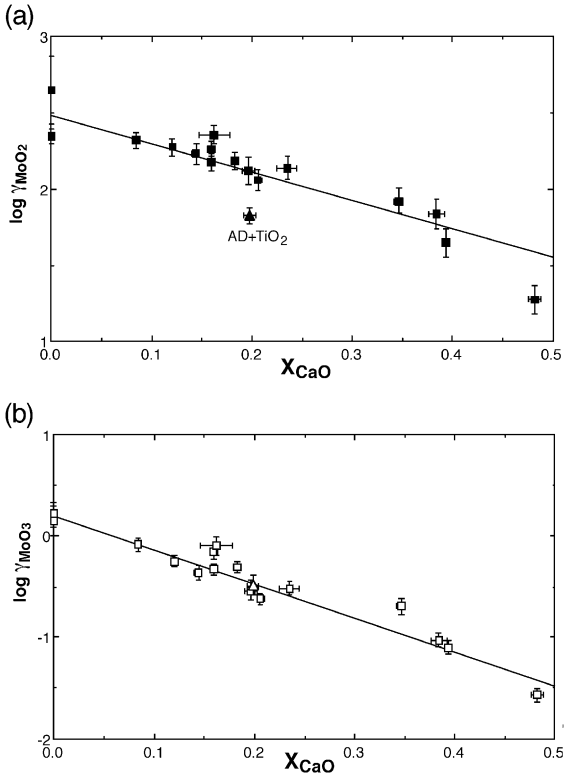

Fig. 5. log $\gamma_{MoO_2}^{sil\ melt}$ and log $\gamma_{MoO_3}^{sil\ melt}$ versus X_{CaO}. Although the correlations are good, this simple relationship does not fit the data within the estimated uncertainties (error bars are two standard deviations). Comparison of the trends of these two figures indicates that the anomalous result for the TiO_2-rich composition (shown as a triangle symbol) implied in Fig. 4 is due to the effect of TiO_2 on $\gamma_{MoO_2}^{sil\ melt}$ and not $\gamma_{MoO_3}^{sil\ melt}$.

formalism has the algebraic form (cf. Helffrich and Wood, 1989):

$$\ln \gamma_i^{\infty} = \sum_{j=1}^{n} \sum_{k=1}^{j} a_{jk} X_j X_k \tag{13}$$

For a system containing n major-element components, there are thus $1/2n(n+1)$ terms in this equation (thus, 10 in CMAS). Here, we used the following simplified equation:

$$\log \gamma_{MoO_{x/2}}^{sil\ melt} = a_1 (X_{CaO})^2 + a_2 (X_{MgO})^2 + a_3 (X_{CaO} X_{MgO}) + a_0 \tag{14}$$

where, with reference to the usual notation (e.g., Helffrich and Wood, 1989):

$$a_1 \equiv \frac{W_{\mathrm{Mo}^{x+}-\mathrm{Ca}}}{2.303RT} \quad (15)$$

$$a_2 \equiv \frac{W_{\mathrm{Mo}^{x+}-\mathrm{Mg}}}{2.303RT} \quad (16)$$

$$a_3 \equiv \frac{(W_{\mathrm{Mo}^{x+}-\mathrm{Ca}} + W_{\mathrm{Ca}-\mathrm{Mo}^{x+}} + W_{\mathrm{Mo}^{x+}-\mathrm{Mg}} + W_{\mathrm{Mg}-\mathrm{Mo}^{x+}} - W_{\mathrm{Ca}-\mathrm{Mg}} - W_{\mathrm{Mg}-\mathrm{Ca}})}{2 \times 2.303RT} \quad (17)$$

and all the possible W parameters involving Al and Si are zero. The inclusion of the constant term a_0 is an ad hoc device to compensate for these neglected terms in Al and Si. It may also serve to account for any systematic errors in the standard state data.

The equation provides an excellent fit to both $\gamma^{\mathrm{sil\ melt}}_{\mathrm{MoO_2}}$ and $\gamma^{\mathrm{sil\ melt}}_{\mathrm{MoO_3}}$, with values of χ^2_ν of 1.6 and 2.7, respectively (see Table 8). It is notable that the values of a_1 and a_2, corresponding to $W_{\mathrm{Mo}^{x+}}-\mathrm{Ca}$ and $W_{\mathrm{Mo}^{x+}}-\mathrm{Mg}$, are both negative. This contrasts with the positive values of W parameters generally encountered in solid solutions, at least in the absence of order–disorder effects. These positive deviations from ideality are related to size mismatch between the substituting species (e.g., Davies and Navrotsky, 1983). It is this size-mismatch effect in crystals that underlies the lattice-strain theory of trace-element partition coefficients (e.g., Brice, 1975; Blundy and Wood, 1991, 1994). The negative values of the W parameters found here point rather to a different phenomenon to that operating in melts, more akin to complex formation. This and its implications will be discussed further below.

Table 8
Results of fitting the activity coefficients of MoO_2 and MoO_3 as a function of composition to the equation:

$\log \gamma^{\mathrm{sil\ melt}}_{\mathrm{MoO}_{x/2}} = a_1(X_{\mathrm{CaO}})^2 + a_2(X_{\mathrm{MgO}})^2 + a_3(X_{\mathrm{CaO}}X_{\mathrm{MgO}}) + a_0$

Parameter	MoO_2	MoO_3
a_1	−5.24 (24)	−7.93 (25)
a_2	−1.73 (38)	−1.33 (53)
a_3	−2.51 (58)	−8.07 (73)
a_0	2.53 (3)	0.24 (4)
χ^2_ν	1.59	2.75

The anomalous TiO_2-rich datum could be interpreted as indicating a Mo^{4+}–Ti complex, but we can think of no chemical justification for the existence of such a complex. Rather, it seems that a different mechanism must be operating here. The Ti in the silicate melt has the same charge (4+) and ionic radius as Mo^{4+}, and therefore the presence of Ti as a major constituent of the melt should define locations in the melt structure, analogous to crystallographic sites, with the appropriate chemical environment for Mo^{4+}.

To put these results in perspective, natural basaltic magmas (sensu lato) have X_{CaO} ranging from ~0.05 (peridotitic komatiites, some lamproites) to ~0.20 (melilitites, ankaramites). This is rather less than the range of X_{CaO} used in our experiments, but is still sufficient to cause $\gamma^{\mathrm{sil\ melt}}_{\mathrm{MoO_3}}$ to vary by nearly an order of magnitude, for example. Our results qualitatively show a similar trend to that found by Walter and Thibault (1995) from their metal/silicate-melt partitioning experiments for Mo, but quantitatively, we cannot account for the two orders-of-magnitude variation in partition coefficients that they observed. Moreover, their melt compositions varied mainly in MgO content, not CaO, and from our results, this should have a much less dramatic effect.

3.3. Fe, Ni and Co activity coefficients

Activity coefficients for Fe, Ni and Co were calculated via Eq. (8) and using the analytical data in Tables 1, 3 and 4) are given in Table 5. For Ni and Co, the weighted means of the LA-ICP-MS and electron microprobe analyses were used, assuming a weight of ±3%, one standard deviation, for the LA-ICP-MS results, and the empirically observed standard deviation of the electron microprobe analyses (Table 3). The standard deviations of $\gamma^{\mathrm{sil\ melt}}_{\mathrm{NiO}}$ and $\gamma^{\mathrm{sil\ melt}}_{\mathrm{CoO}}$ quoted in Table 5 are the standard errors of these weighted means, and are about 2.5%, and are entirely from propagation of the analytical errors. They do not include systematic errors (e.g., in the standard state thermochemical data) or the uncertainties in measured fO_2.

The values of $\gamma^{\mathrm{sil\ melt}}_{\mathrm{FeO}}$, $\gamma^{\mathrm{sil\ melt}}_{\mathrm{NiO}}$, and $\gamma^{\mathrm{sil\ melt}}_{\mathrm{CoO}}$ vary by about a factor of two as a function of melt composition, much less than the variation in $\gamma^{\mathrm{sil\ melt}}_{\mathrm{MoO_2}}$ and $\gamma^{\mathrm{sil\ melt}}_{\mathrm{MoO_3}}$. For most compositions, the values of $\gamma^{\mathrm{sil\ melt}}_{\mathrm{FeO}}$ cluster around 1.3, that is, tending towards

small positive deviations from ideality; values of $\gamma_{CoO}^{sil\ melt}$ are around 1.0, or approximately ideal; and values of $\gamma_{NiO}^{sil\ melt}$ are around 2.5.

The remarkable feature of the results is that all three activity coefficients depend on melt composition in more or less the same way, which can be illustrated by plotting one against another, as in Fig. 6a,b. These correlations indicate that there is some fundamental chemical property of the melts that controls the value of the activity coefficients of these compatible elements. Unfortunately, it is not clear what this property is. There is no obvious correlation with any simple compositional variable such as X_{CaO} or X_{MgO}, in contrast to the behaviour of $\gamma_{MoO_2}^{sil\,melt}$ and $\gamma_{MoO_3}^{sil\,melt}$, therefore, the four-parameter fit used successfully to describe the compositional dependence of $\gamma_{MoO_2}^{sil\ melt}$ and $\gamma_{MoO_3}^{sil\ melt}$ does not describe the variation in $\gamma_{FeO}^{sil\ melt}$, $\gamma_{NiO}^{sil\ melt}$ or $\gamma_{CoO}^{sil\ melt}$ adequately. It is possible to fit the data for all three oxides quite well using a full subregular solution model (Eq. (13)), but this has 10 terms, and to use a 10-term model to fit 18 data is not very satisfying intellectually. The fits to the Ni and Co data are good, with χ_v^2 of 3.1 and 1.3, respectively. The parameters for these fits are given in Table 9, not because we believe they have much general significance, but because they provide a way to compare our results with previous work. For the Fe data, the value of χ_v^2 is 17.7, which may reflect an over-optimistic assessment of the analytical errors, or perhaps somewhat greater complexity in the solution properties of FeO in silicate melts.

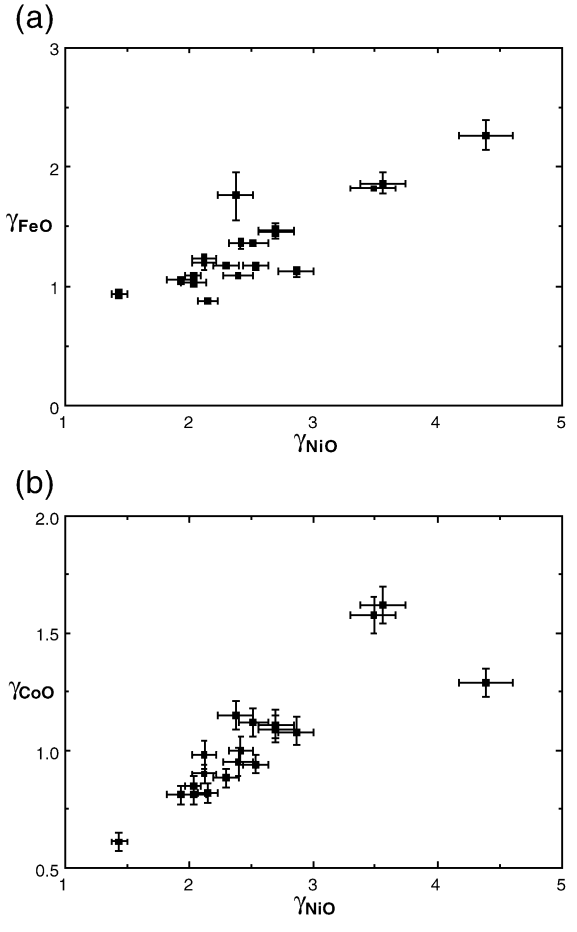

Fig. 6. Correlation of (a) $\gamma_{FeO}^{sil\ melt}$ with $\gamma_{NiO}^{sil\ melt}$, and (b) $\gamma_{CoO}^{sil\ melt}$ with $\gamma_{NiO}^{sil\ melt}$.

Table 9
Coefficients from the fitting of $\gamma_M^{sil\ melt}$ to the polynomial expression: $\ln \gamma_M^{sil\ melt} = \Sigma_{j=1}^{4}\ \Sigma_{k=1}^{j}\ a_{jk}X_jX_k$

	X_{Ca}	X_{Mg}	X_{Al}	X_{Si}
Ni (χ_v^2 = 3.1)				
X_{Ca}	6.26	14.97	18.77	− 10.23
X_{Mg}		7.92	11.68	− 10.47
X_{Al}			− 5.74	− 2.46
X_{Si}				5.19
Co (χ_v^2 = 1.34)				
X_{Ca}	5.99	13.21	16.62	− 11.43
X_{Mg}		2.59	12.27	− 9.37
X_{Al}			− 1.62	− 6.59
X_{Si}				3.67
Fe (χ_v^2 = 17.7)				
X_{Ca}	6.62	16.30	3.74	− 8.50
X_{Mg}		6.09	− 3.21	− 7.34
X_{Al}			− 2.61	6.08
X_{Si}				1.16

It would be interesting to know if the variation in $\gamma_{FeO}^{sil\ melt}$, $\gamma_{NiO}^{sil\ melt}$, and $\gamma_{CoO}^{sil\ melt}$ with melt composition correlated with the variation in the activity coefficient of the major component MgO. Although, as yet, neither direct measurement nor thermodynamic modelling of phase equilibrium data can yield values of $\gamma_{MgO}^{sil\ melt}$ with the required accuracy for the range of melt compositions used in this study, the well-known lack of a significant compositional dependence for the distribution of Fe^{2+} and Mg between olivine and melt ($KD_{Fe-Mg}^{ol/melt}$) shows that $\gamma_{MgO}^{sil\ melt}$ is indeed well correlated with $\gamma_{FeO}^{sil\ melt}$ for that subset of melt compositions

that are in equilibrium with olivine. This point was made previously by Roeder (1974).

There are also some real anomalies that fall off the correlations shown in Fig. 6a,b. For the CAS3 composition, which stands out from the other compositions on account of its very high silica and high alumina, the values of both $\gamma_{FeO}^{sil\ melt}$ and $\gamma_{NiO}^{sil\ melt}$ stand out as the highest of any composition studied, whereas $\gamma_{CoO}^{sil\ melt}$ for this composition appears average. The CAS3 composition is the nearest thing to a granitic type of composition used in this study. Among the Fe data, $\gamma_{FeO}^{sil\ melt}$ for the composition CMAS-D seems unusually high, for no obvious reason. This result has been checked in the course of a parallel study (O'Neill, unpublished data) and appears real. These exceptions suggest that further complexity would emerge if the compositional range studied were to be enlarged. Such a study would seem worthwhile in that more data may yet reveal a pattern that is not presently apparent.

4. Comparison with previous experimental studies

4.1. Mo

The solubility of Mo in anorthite–diopside eutectic melt was previously measured by Holzheid et al. (1994) using the same experimental method as here (wire loops) at 1400 °C, but with fO_2 controlled by H_2–CO_2–N_2 gas mixtures rather than CO–CO_2, and with samples analysed by instrumental neutron activation. The results of their study are compared with the present work in Fig. 7. Holzheid et al. (1994) also studied the solubility of Ni and Co in the same experiments. When their results for all three elements are compared with ours, it becomes apparent that the discrepancy illustrated in Fig. 7 may largely be due to a systematic difference in oxygen fugacity between their experiments and ours. For the Mo solubilities, this would seem to be about 0.2 log units in fO_2. For Ni and Co, the values of $\gamma_{NiO}^{sil\ melt}$ and $\gamma_{CoO}^{sil\ melt}$ calculated from the equations for the solubilities as a function of fO_2 given in Table 2 of Holzheid et al. (1994) for the fO_2s used here ($10^{-9.6}$ and $10^{-11.63}$, respectively) are 3.9 and 1.7, respectively, versus 2.5 and 1.1 in this study. This translates into a discrepancy of 0.4 in log fO_2.

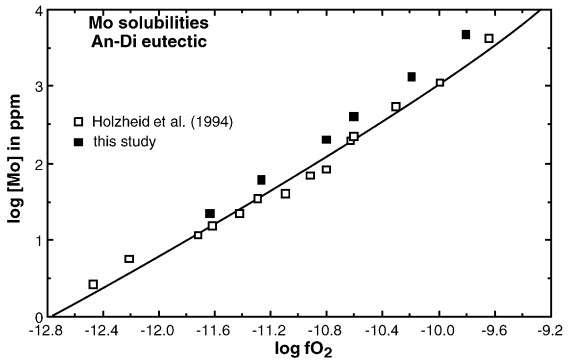

Fig. 7. Comparison of the results of this study on the solubility of Mo in anorthite–diopside eutectic composition at 1400 °C with those of Holzheid et al. (1994). The curve is the best fit by least squares of the data of Holzheid et al. (1994) to Eq. (10).

The later results of Holzheid et al. (1997) for Fe as well as Ni and Co are closer to ours, and are generally consistent within a putative discrepancy of ~ 0.1 in log fO_2. An important aspect of the work of Holzheid et al. (1996, 1997) is that they demonstrate experimentally that the presence of substantial amounts of FeO in the silicate melt has little effect on $\gamma_{NiO}^{sil\ melt}$ and $\gamma_{CoO}^{sil\ melt}$.

4.2. NiO

There has probably been more work on the thermodynamic properties of Ni in silicate melts than all other trace elements put together. In part, this reflects the importance that the Ni content of a magma plays in constraining the amount of low-pressure olivine fractionation that it may have undergone; hence, how close it may be to a primitive melt from the mantle. The high Ni abundance of the mantle may itself hold clues bearing on the accretion of the Earth and its fundamental differentiation into core and mantle. These are all topics whose quantitative understanding from the petrological perspective requires knowledge of the thermodynamic properties of Ni in silicate melts.

However, in part, the experimental interest in Ni is no doubt helped by the way Ni lends itself to the type of experimental approach used in this study. NiO activities in silicate melts have also been investigated extensively in the metallurgical and ceramics literature (e.g., Grimsey and Biswas,

1976, 1977; Lacy and Pask, 1970), but on melt compositions so far removed from either natural magmas or the synthetic compositions used here as to prevent meaningful comparison. We therefore discuss only that part of the literature bearing on geologically relevant melt compositions. We will not discuss the large literature on various crystal/melt partition coefficients of Ni, as it is not possible to disentangle the effects of melt composition on $\gamma_{NiO}^{sil\ melt}$ from other variables. Nor do we discuss experiments on metal/melt partition coefficients in which the composition of the metal is not Ni-rich, as in these experiments, the effect of melt composition is usually obscured by the uncertainties in calculating the activity of Ni in the metal. This still leaves a fair number of studies (Campbell et al., 1979; Doyle and Naldrett, 1987; Dudson and Fraser, 1981; Pretorius and Muan, 1992; Snyder and Carmichael, 1992; Holzheid et al., 1994, 1997; Dingwell et al., 1994; Ertel et al., 1997).

At first sight, most of these studies appear to report values of $\gamma_{NiO}^{sil\ melt}$ much greater than those found in this study (i.e., $2>\gamma_{NiO}^{sil\ melt}<5$). This is due to a choice of solid NiO as the standard state, compounded by the use of older thermodynamic data for the Ni–NiO(s) equilibrium. We have therefore converted all quoted results to the standard state of liquid NiO used here, using the thermodynamic data in Table 6. From Eq. (8), it can be seen that changing the standard state requires only that the reported value of $\gamma_{NiO}^{sil\ melt}$ be multiplied by a factor that depends on temperature. A systematic error in oxygen fugacity, which is the most likely error experimentally, also results in changing $\gamma_{NiO}^{sil\ melt}$ by a constant factor at constant temperature. Many of the studies have much higher levels of NiO in the melt than used here, but this does not seem to be an issue as $\gamma_{NiO}^{sil\ melt}$ remains constant within the accuracy of these studies to surprisingly high values (at least 10 wt.% NiO—e.g., Lacy and Pask, 1970; Doyle and Naldrett, 1987).

Campbell et al. (1979) studied Ni solubilities in a range of melt compositions from basalt to dacite, using essentially the same wire loop techniques as used here, at 1200–1400 °C. Because their melt compositions were based on natural melts, they contained FeO as a significant component. This introduces the additional experimental complexity that Fe partitions into the Ni metal. However, the amount of Fe in the metal is small (~ 2%), and Campbell et al. demonstrated that local equilibrium at the wire's interface with the melt was reached by calculating values of $\gamma_{FeO}^{sil\ melt}$ that appear reasonable (and in good agreement with the range of values found in this study). Alkali loss from the starting compositions was another problem, and this resulted in the final compositions of the melts being more siliceous than intended: for example, the dacite ended up more akin to a peraluminous rhyolite. The values of $\gamma_{NiO}^{sil\ melt}$ reported by Campbell et al. need to be multiplied by factors of 0.23 at 1200 °C, 0.31 at 1300 °C and 0.41 at 1400 °C to adjust them to the standard state of this study. This removes the large temperature dependence shown by Campbell et al. (Note that the simplest behaviour of an activity coefficient with temperature that is expected from basic thermochemical principles is for the quantity RT log γ to be independent of temperature, rather than γ itself. This is because constant RT log γ implies a constant excess enthalpy of mixing and zero excess entropy of mixing, whereas a constant γ would require a nonzero excess entropy of mixing.) For the basaltic compositions studied, the recalculated values of $\gamma_{NiO}^{sil\ melt}$ are quite similar to the range found here (i.e., about 2.5—see Fig. 6a,b). However, the recalculated value for the extreme "dacite" composition is ~ 9 at 1400 °C, substantially higher than even the most silica-rich composition in this study (CAS3). Snyder and Carmichael (1992) also investigated seven FeO-containing natural basaltic compositions in equilibrium with Ni–Fe metal wire between 1395 and 1562 K, but their reported values of $\gamma_{NiO}^{sil\ melt}$ are much greater than those of other studies for basaltic or near-basaltic compositions, being in the range 6.7–18.3 when corrected to our standard state.

Dingwell et al. (1994) used a variation on the experimental approach of this study, namely the stirred crucible method. They investigated a silicate melt composition consisting of the anorthite–diopside eutectic plus 10% CaO. Later, Ertel et al. (1997) used the same method to study the effect of changing the melt composition. They investigated three joins, each starting with the anorthite–diopside eutectic composition, to which progressive amounts of Mg_2SiO_4, SiO_2 and Na_2SiO_3 were added to the

stirred crucible. They found little change of solubility along the first two joins, in good agreement with the results of this study for the compositions AD eutectic, AD + Fo, and AD + Qz (Table 3). Values of $\gamma_{NiO}^{sil\ melt}$ derived from their experiments are about 3.2, versus 2.8 in this study. In contrast, they observed quite marked changes in Ni solubility along the join AD eutectic–Na_2SiO_3, with the solubility of Ni first decreasing then increasing as Na_2SiO_3 was added. This suggests that further investigation of the effect of alkalis would uncover some interesting behaviour. The stirred crucible method, although tedious compared to the wire-loop technique used in this paper, has the advantage that alkali loss by evaporation is kept to reasonable levels, although it is not entirely negligible.

The closest of the previous Ni studies in aims to this one are those of Dudson and Fraser (1981) and Pretorius and Muan (1992). Dudson and Fraser investigated a wide range of compositions in the CMAS system, including some in the CaO–MgO–SiO_2 (CMS) ternary subsystem. They too used the wire loop method, but with CO_2–H_2 gas mixtures at 1445 °C. Dudson and Fraser report their results relative to a standard state of solid NiO; to convert their reported values of $\gamma_{NiO}^{sil\ melt}$ at 1445 °C to the standard state used here, multiply by 0.57. Their corrected results for $\gamma_{NiO}^{sil\ melt}$ range from 1.3 for $CaMgSi_2O_6$ (diopside melt) to 2.6 for a couple of high Ca, high Al compositions. Dudson and Fraser found that their Al-free compositions (like $CaMgSi_2O_6$) consistently gave lower values of $\gamma_{NiO}^{sil\ melt}$, but beyond this were unable to discern any consistent pattern in their data—which must unfortunately also be the conclusion of this study.

To compare quantitatively the data of Dudson and Fraser (1981) with the results of this study, we have calculated values of $\gamma_{NiO}^{sil\ melt}$ for the compositions used by Dudson and Fraser at 1445 °C using the fit of our data at 1400 °C to the subregular formalism (Eq. (13); parameters in Table 9). The resulting calculated values are compared to the observed values (corrected to the same standard state of liquid NiO) in Fig. 8a. There is a fair correlation, although clearly the calculated values are systematically higher. The small temperature difference between the two sets of data is not sufficient to account for this; rather, the discrepancy is probably due to a systematic difference in the measurement of oxygen fugacity between our experiments and those of Dudson and Fraser. Least squares regression of the calculated versus the observed values gives

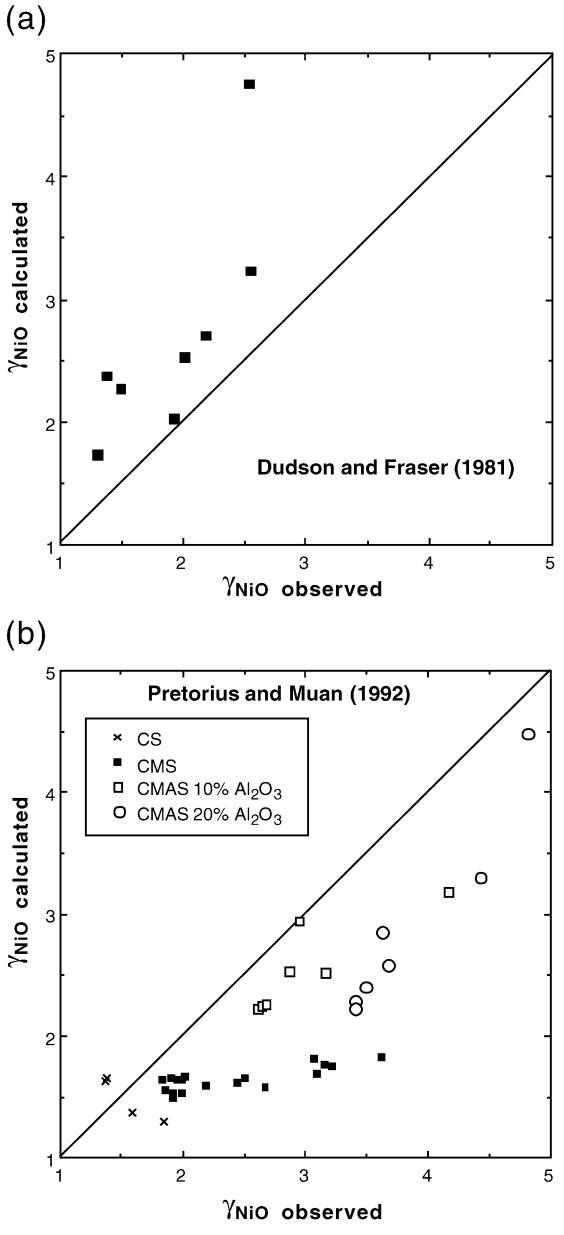

Fig. 8. Comparison of previous measurements of $\gamma_{NiO}^{sil\ melt}$ in CMAS melts with $\gamma_{NiO}^{sil\ melt}$ predicted from the results of the present study, using the fit to Eq. (13) given in Table 9. (a) Dudson and Fraser (1981) at 1445 °C; (b) Pretorius and Muan (1992) at 1400 °C.

a factor of 1.36, which corresponds to an average discrepancy of 0.27 in log fO_2.

The relatively low values of $\gamma_{NiO}^{sil\ melt}$ in Al-free systems found by Dudson and Fraser were confirmed by Pretorius and Muan (1992), who studied compositions in the Al-free CMS ternary, and with 10% and 20% Al_2O_3 added, at 1400 °C (the same temperature as this study). These authors also report their results relative to a standard state of solid NiO, using an even older calibration of the Ni–NiO(s) equilibrium, which requires a correction factor at 1400 °C of 0.39. The comparison between their corrected observed values and those calculated from Eq. (13) (Table 9) is shown in Fig. 8b. Two points need to be made. Firstly, the observed values are displaced relative to the calculated values in the opposite sense to those of Dudson and Fraser (1981); the best-fit correction factor, considering only the 10% and 20% Al_2O_3 data, is 0.78, implying a discrepancy of 0.21 in fO_2. In addition to this, there is an obvious systematic discrepancy depending on the Al_2O_3 content, implying that our empirical fit to our 18 compositions cannot even provide a satisfactory general description of the CMAS system.

Pretorius and Muan (1992) also investigated the effect of adding 5–7.5 wt.% K_2O to their CMS compositions. The resulting values of $\gamma_{NiO}^{sil\ melt}$ are indistinguishable from those in the CMS system, indicating a negligible effect of K_2O, at least in the absence of any Al_2O_3 in the system. This is in contrast to the results of Ertel et al. (1997) on the effect of adding Na_2SiO_3 to AD eutectic, but at present, there are insufficient data on the effects of the alkalis to warrant any general conclusions.

Doyle and Naldrett (1987) investigated a quasi-ternary system that they described as "Matrix–NiO–MgO" where "Matrix" is a $\gamma_{NiO}^{sil\ melt}$ composition in the CAS–TiO_2–K_2O system with about 1% TiO_2 and 2–4% K_2O. They employed three fO_2 conditions, corresponding to values of the activity of NiO (a_{NiO}) of 0.096, 0.196 and 0.297, respectively (recalculated to our standard state), at 1400 °C. There is no discernible difference in values of $\gamma_{NiO}^{sil\ melt}$ calculated from the different fO_2s; thus, their results can be projected onto a quasi-binary between "Matrix" and MgO. Their results are summarized in this way in Fig. 9. Adding MgO to the "Matrix" composition does not seem to have any effect either; hence, in the absence of any systematic compositional trends, the scatter in their data must be ascribed to experimental noise. The mean of all their data is 2.78, with an uncertainty of ± 0.25. To put this uncertainty into an experimental context $\gamma_{NiO}^{sil\ melt}$, it corresponds to an uncertainty in log fO_2 of ± 0.05, coupled with an analytical uncertainty for Ni in the melt of ± 5%. From our experience, these are quite reasonable experimental uncertainties, and this makes the point that a high degree of experimental precision is needed for studying the "fine structure" of the variation of $\gamma_{NiO}^{sil\ melt}$ with melt composition.

To compare further the results of Doyle and Naldrett (1987) with ours, we have projected their compositions onto the CMAS system by subtracting TiO_2 and K_2O and recalculating to 100%. The comparison is given in Fig. 9. The fit to our results predicts that adding MgO should cause a decrease of $\gamma_{NiO}^{sil\ melt}$, but, as noted above, this is not evident in the results of Doyle and Naldrett. Perhaps, it is lost in the experimental noise. Nevertheless, the mean value of $\gamma_{NiO}^{sil\ melt}$ from the results of Doyle and Naldrett agrees quite well with the average of our predicted values.

In conclusion, there is good agreement that values of $\gamma_{NiO}^{sil\ melt}$ in basaltic melts fall in the range 2.5–3.5 at

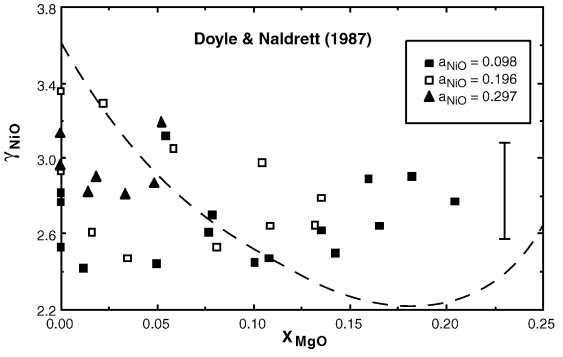

Fig. 9. Comparison of measurements of $\gamma_{NiO}^{sil\ melt}$ of Doyle and Naldrett (1987) at three different values of a_{NiO} as a function of X_{MgO} in the quasi-ternary system "Matrix"–MgO–NiO, with the predicted dependence of $\gamma_{NiO}^{sil\ melt}$ on melt composition from the present study (shown as the dashed curve). The present results predict that $\gamma_{NiO}^{sil\ melt}$ should decrease with X_{MgO} at least to $X_{MgO} = 0.15$, which is not seen in the results of Doyle and Naldrett. In fact, the data of Doyle and Naldrett show no discernible dependence on composition. The observed scatter is equivalent to experimental uncertainties of ± 0.05 in log fO_2 combined with ± 5% in Ni analyses, shown as the error bar.

1400 °C when normalized to a standard state of liquid NiO. Only the study of Snyder and Carmichael (1992) disagrees with this generalization. As shown by Holzheid et al. (1997), any temperature dependence is modest when $\gamma_{NiO}^{sil\ melt}$ is calculated relative to the liquid standard state. However, variations of $\gamma_{NiO}^{sil\ melt}$ within the observed range are real and not just from experimental noise, as demonstrated in this study by the correlations between $\gamma_{NiO}^{sil\ melt}$ and $\gamma_{FeO}^{sil\ melt}$ or $\gamma_{CoO}^{sil\ melt}$. Hence, modelling of $\gamma_{NiO}^{sil\ melt}$ as a function of melt composition may be required for some quantitative petrological applications. There is evidence suggesting that extremely siliceous melts may have larger values of $\gamma_{NiO}^{sil\ melt}$ (e.g., Campbell et al., 1979), but this requires further work. It is also unfortunately apparent that systematic inter-laboratory differences in the measurement of oxygen fugacity are of the order of 0.2 in $\log f O_2$, and in many previous studies precision was not much better. This introduces uncertainties that are large enough to frustrate the idea of pooling the results of all the different studies to provide an expanded range of melt compositions on which a general model might be based.

4.3. FeO

Surprisingly, given its importance as a major component in natural magmas, there has been less work on the thermodynamic properties of FeO than NiO in silicate melts in the geological literature. This imbalance is somewhat rectified by the wealth of information on the activities of FeO in slags in the metallurgical literature, but this work has concentrated on simple systems generally without Al_2O_3 or MgO as major components. Recent results on CMAS–FeO slags (see, for example, Liu et al., 2001) cover compositions much poorer in silica than those of geological interest or used in this study. In the geological literature, we are aware only of the studies of Roeder (1974), Doyle and Naldrett (1986), Doyle (1988, 1989), and Holzheid and Palme (1996) and Holzheid et al. (1997) as providing suitable comparisons with our data.

Roeder (1974) reported 47 results on natural basaltic compositions between 1150 and 1306 °C using the "stirred crucible" method. Roeder reported his results relative to a standard state of liquid FeO, using thermodynamic data so close to those used here that no correction is needed. His reported values of $\gamma_{FeO}^{sil\ melt}$ range from 0.79 to 2.00, virtually identical to the range found here.

The series of studies by Doyle and Naldrett (1986) and Doyle (1988, 1989) using the wire-loop method contains a wealth of data at one temperature (1327 °C), on relatively simple systems quite closely comparable in composition to those investigated here. One valuable difference is that the Doyle experiments investigated several different values of $a_{FeO}^{sil\ melt}$ rather than just the single value of $a_{FeO}^{sil\ melt}$ of this study, and thus cover a large range of FeO concentrations. They show unequivocally that the relationship between FeO concentration and $\gamma_{FeO}^{sil\ melt}$ is very simple, with $\gamma_{FeO}^{sil\ melt} \rightarrow 1$ perfectly smoothly as $X_{FeO} \rightarrow 1$. In what follows, we have converted results from all three of the Doyle studies to our choice of standard state (Table 9). Also, Doyle and Naldrett (1986) report mole factions using moles of Al_2O_3, K_2O and Na_2O rather than the single-cation convention we use here (i.e., $AlO_{1.5}$, $KO_{0.5}$, $NaO_{0.5}$), and we have accordingly converted their reported mole fractions to our convention. This increases $\gamma_{FeO}^{sil\ melt}$ by nearly 10% for their compositions.

Doyle and Naldrett (1986) studied three systems of the type "Matrix–MgO–FeO" in which the "Matrix" is composed of a $CAS \pm TiO_2 \pm K_2O \pm Na_2O$ composition based on a standard diabase, an average mid-ocean ridge basalt (MORB), and a high-Ti lunar mare basalt, respectively. Much of the Na_2O and some of the K_2O were lost by volatilization during the experiments; hence, these components are of minor importance in the final compositions and the systems are similar to the CMAS–FeO ($\pm TiO_2$) systems of this study, except, as mentioned above, that their study extends to far higher FeO contents ($\sim$ 60 wt.% FeO). The main difference between the first two systems is that the "diabase" is slightly higher in silica content than the "MORB". Because the systems have only two degrees of compositional freedom (since Matrix + MgO + FeO must add up to 100%), it is easy to check the data for any systematic variations of $\gamma_{FeO}^{sil\ melt}$ with composition (e.g., X_{MgO} or X_{FeO} or the product of both). When the "diabase" and the "MORB" systems are considered together, no consistent pattern of compositional variation is discernible, and each quasi-ternary systems can be fitted to a single value of $\gamma_{FeO}^{sil\ melt}$; for the "diabase" system,

the fit gives $\gamma_{FeO}^{sil\ melt} = 1.16 \pm 0.10$ (77 data) and for the "MORB" system $\gamma_{FeO}^{sil\ melt} = 1.24 \pm 0.09$ (88 data). These values are obviously identical within uncertainty and are moreover in excellent agreement with the results of this study for similar compositions. The uncertainty is about 9%, which is the same as Doyle and Naldrett (1987) obtained in their study on a "Matrix–MgO–NiO" system (see above). This magnitude of uncertainty would derive from an experimental uncertainty in log fO_2 of ± 0.05 and in analysis of $\pm 5\%$, relative.

By contrast, the results of Doyle and Naldrett (1986) for their quasi-ternary high-Ti mare basalt system do show some systematic variations of $\gamma_{FeO}^{sil\ melt}$ with composition. The value of $\gamma_{FeO}^{sil\,melt}$ for the compositions poorest in MgO and FeO is only ~ 0.75, and increases slightly with both MgO and FeO. The increase of $\gamma_{FeO}^{sil\ melt}$ with FeO is expected from the requirement that $\gamma_{FeO}^{sil\,melt} \rightarrow 1$ as $X_{FeO} \rightarrow 1$ (Raoult's law), if experimental conditions and standard state thermodynamic data are all internally consistent. The salient result, that TiO_2 lowers $\gamma_{FeO}^{sil\ melt}$, confirms the inference from our one TiO_2-containing composition. The mean value of $\gamma_{FeO}^{sil\ melt}$ for all 53 data in this system is 0.85 ± 0.09.

Doyle (1988) studied the system CAS–FeO $\pm$ K_2O, using four subsystems each characterized by one $KAlO_2/SiO_2$ ratio and with varying amounts of $CaAl_2Si_2O_8$, SiO_2 and FeO. One hundred twenty-five data were reported. The data from the subsystem with zero $KAlO_2$ shows a good positive correlation between $\gamma_{FeO}^{sil\,melt}$ and $CaAl_2Si_2O_8$ (equivalent to a negative correlation with SiO_2), but because of the covariance of CaO, Al_2O_3, and SiO_2, it is not possible to deduce which oxide component this depends on. Nevertheless, this is a trend that is not apparent in the CMAS compositions of this study. Increasing $KAlO_2$ causes $\gamma_{FeO}^{sil\ melt}$ to increase.

Later, Doyle (1989) reported another extensive series of experiments (164 data) on three quasi-quaternary subsystems within the system CAS–FeO–$TiO_2 \pm K_2O$. Again, each subsystem is characterized by a different concentration of a $KAlO_2$ component, and has varying amounts of $CaAl_2Si_2O_8$, SiO_2, FeO and TiO_2. Although, broadly speaking, the results are quite similar to the others reported by Doyle and Naldrett (1986) and Doyle (1988), in that values of $\gamma_{FeO}^{sil\ melt}$ hover around unity, in detail they show some compositional trends that are difficult to reconcile with previous observations. The quasi-quaternary with zero $KAlO_2$ shows almost no decrease of $\gamma_{FeO}^{sil\ melt}$ with TiO_2 as X_{TiO_2} increases from 0 to 0.15, although $\gamma_{FeO}^{sil\,melt}$ does increase with FeO as in the study of Doyle and Naldrett (1986). Values of $\gamma_{FeO}^{sil\ melt}$ increase with increasing amounts of $KAlO_2$, as also found in the study of Doyle (1988).

Wire-loop experiments using Fe–Ni and Fe–Ni–Co alloys have been reported by Holzheid and Palme (1996) and Holzheid et al. (1997). These experiments necessarily introduce an additional source of error since the composition of the alloy has to be determined. Two compositions (AD eutectic and tholeiitic basalt) were investigated over a range of temperatures. The results give values of $\gamma_{FeO}^{sil\ melt}$, $\gamma_{NiO}^{sil\ melt}$, and $\gamma_{CoO}^{sil\ melt}$ that are about 25% higher than in this study and those of Doyle and Naldrett (1986, 1987) and Doyle (1988, 1989), which is probably due to a systematic difference either in activity coefficients in the metal phase, or in measurement of fO_2. Nevertheless, the work of Holzheid et al. (1997) is particularly valuable in confirming a conclusion previously reached by Roeder (1974), that is $\gamma_{FeO}^{sil\ melt}$ almost independent of temperature when referred to the standard state of liquid FeO.

The values of $\gamma_{FeO}^{sil\ melt}$ reported by Snyder and Carmichael (1992) from experiments with Fe–Ni alloys are aberrant compared to the results from all other studies, even when corrected to the same standard state.

5. Discussion

5.1. Mo^{4+}/Mo^{6+} ratios in silicate melts

The ratio of Mo^{6+} to Mo^{4+} in a silicate melt is given by the reaction:

$$MoO_2 + 1/2\ O_2 = MoO_3 \tag{18}$$

For which at equilibrium:

$$\frac{X_{MoO_3}^{sil\ melt}}{X_{MoO_2}^{sil\ melt}} = \frac{[Mo^{6+}]}{[Mo^{4+}]} = (fO_2)^{1/2} \cdot \frac{\gamma_{MoO_2}^{sil\ melt}}{\gamma_{MoO_3}^{sil\ melt}} \cdot \exp\{-\Delta_r G^{o}_{(T,\ 1\ bar)}/RT\} \tag{19}$$

where:

$$\Delta_r G^o_{(T,\ 1\ bar)} = \Delta_f G^o_{(T,\ 1\ bar)}(MoO_3) - \Delta_f G^o_{(T,\ 1\ bar)}(MoO_2) \quad (20)$$

The ratio may also be calculated from the experimental results (Table 5) using:

$$\frac{[Mo^{6+}]}{[Mo^{4+}]} = (fO_2)^{1/2} \cdot \frac{Q^{MoO_3}}{Q^{MoO_2}} \quad (21)$$

For many purposes, it is enlightening to know the fraction of total Mo that is Mo^{4+}, defined as $[Mo^{4+}]/[Mo^{4+} + Mo^{6+}]$ or $[Mo^{4+}]/[\sum Mo]$, as a function of $\log fO_2$. Rearrangement of Eq. (19) gives:

$$\frac{[Mo^{4+}]}{[\sum Mo]} = \frac{1}{1 + \exp\left\{-\frac{1}{2}\log fO_2 + \Delta_r G^o_{(T,\ 1\ bar)}/2.303RT + \log\frac{\gamma^{sil\ melt}_{MoO_3}}{\gamma^{sil\ melt}_{MoO_2}}\right\}} \quad (22)$$

As an illustration, the fraction of Mo^{4+} is plotted as a function of $\log fO_2$ for two compositions in Fig. 10, relative to some common oxygen buffers. The shape of the curves is completely specified by the stoichiometry of the reaction (i.e., the difference in the valence states of Mo^{4+} and Mo^{6+}) as long as the concentrations of both MoO_2 and MoO_3 are in the Henry's law region; however, the position of the curves relative to the $\log fO_2$ axis depends on $\Delta_r G^o_{(T,\ 1\ bar)}$, which is a constant for all compositions at constant T and P, and the ratio $\gamma^{sil\ melt}_{MoO_2}/\gamma^{sil\ melt}_{MoO_3}$, which may vary with the major-element composition of the melt. Since the shape of the curves is fixed, an entire curve may be specified using just one parameter. A convenient parameter is the oxygen fugacity at which the concentrations of Mo^{6+} and Mo^{4+} are equal, called here $(fO_2)^{eq}$, where, from Eqs. (19) or (22):

$$(fO_2)^{eq} = 2\frac{\gamma^{sil\ melt}_{MoO_3}}{\gamma^{sil\ melt}_{MoO_2}} \cdot \exp\{\Delta_r G^o_{(T,\ 1\ bar)}/RT\} \quad (23)$$

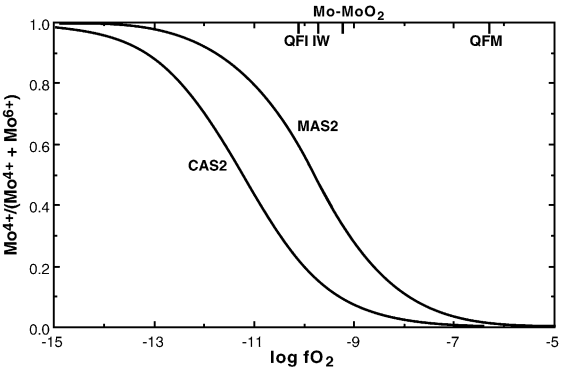

Fig. 10. Proportion of Mo as Mo^{4+} as a function of $\log fO_2$ for two compositions (CAS2 and MAS2, see Table 1), chosen to represent the extremes from the present study. These results indicate that Mo dissolves almost entirely as Mo^{6+} in silicate melts at typical terrestrial oxygen fugacities ($\log fO_2 > QFM-2$), but should be present as both Mo^{4+} and Mo^{6+} in roughly equal amounts in equilibrium with metallic Fe; for example, during core formation in the Earth, or in the lunar environment.

Because the compositional dependence of $\gamma^{sil\ melt}_{MoO_2}$ and $\gamma^{sil\ melt}_{MoO_3}$ are so similar, most of the effects of composition cancel out when their ratios are taken, although there is a small residual effect of composition, which can, within experimental error, be represented as a linear relation between $\log (fO_2)^{eq}$ and X_{CaO}, as shown in Fig. 11.

The valence state of an element can have a profound effect on its crystal/melt partition coefficients. A well-known example is the way that low fO_2 causes reduction of the Rare Earth Element Eu from the typical REE valence state of Eu^{3+} to Eu^{2+}, enabling Eu to substitute readily for Ca in plagioclase. The extent to which the geochemical properties of Mo depend on oxidation state are not known. An important application may be in its effect on the fractionation of Mo from W during metal/silicate partitioning accompanying core formation in planetary bodies. The importance of Mo and W in this context is due to their identity as the only two moderately siderophile elements that are also cosmochemically refractory. This eliminates volatility as a possible cause for their observed depletion in the Earth's mantle, which is therefore presumably due to core formation only (see O'Neill and Palme, 1998, p. 98). Generally, Mo and W share very similar chemical properties, but one difference is that WO_2

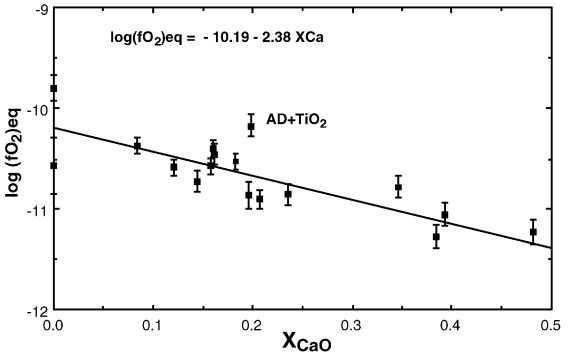

Fig. 11. The fO_2 at which the concentrations of Mo^{4+} and Mo^{6+} are equal, $(fO_2)^{eq}$, as a function of X_{CaO} in the melt.

does not have the high activity coefficients of MoO_2 (Ertel et al., 1996). Hence, at the low fO_2s, appropriate for equilibrium with Fe-rich metal, W occurs in silicate melts almost entirely as W^{4+} whereas, as shown here, Mo is a mixture of Mo^{4+} and Mo^{6+} (Fig. 10). In this regard, the properties of Mo are similar to Re, in which the Re^{6+} oxidation state in silicate melts is also stabilized relative to Re^{4+} by virtue of a much lower value of $\gamma^{sil\ melt}_{ReO_3}$ compared to $\gamma^{sil\ melt}_{ReO_2}$ (Ertel et al., 2001).

5.2. The effect of melt composition on Mo partitioning between clinopyroxene and melt

Hill et al. (2000) measured the part of a large number of trace elements, including Mo, between clinopyroxene and silicate melt at 1218 °C, for four compositions close to the system CMAS. The fO_2 of the experiments is not known exactly, but must be very high, and the oxidation sate of Mo in the silicate melt was probably all 6+. Hill et al. interpreted the variation of $D^{melt/cpx}_{Mo}$ that they observed as due to changing tetrahedrally coordinated Al ($^{iv}Al^{cpx}$) in the clinopyroxene (or Ca-Tschermaks component). But $^{iv}Al^{cpx}$ is almost perfectly negatively correlated with CaO in the melt in these experiments, and measured values of $D^{melt/cpx}_{Mo}$ therefore also show an excellent negative correlation with CaO, as expected from our experimental results. This illustrates well the difficulty in disentangling the different influences on trace-element partition coefficients, discussed in the Introduction. Here, we have a good opportunity to discriminate between the effects of melt composition and crystal composition since we have independently measured the effect of melt composition on $\gamma^{sil\ melt}_{MoO_3}$ (albeit at a slightly different temperature).

Accordingly, we have calculated values of $\gamma^{sil\ melt}_{MoO_3}$ for their reported glass compositions from our fit to our data at 1400 °C given in Table 8 (i.e., the temperature difference has been ignored). The correlation between $D^{melt/cpx}_{Mo}$ and $\gamma^{sil\ melt}_{MoO_3}$ is shown in Fig. 12. It appears that the variation in $D^{melt/cpx}_{Mo}$ is entirely accounted for by the effect of melt composition on $\gamma^{sil\ melt}_{MoO_3}$.

Unfortunately, this minor triumph is a short-lived one, as the experiments of Hill et al. (2000) show that the true HFSE (Zr, Hf, Nb and Ta) in their experiments show the opposite correlation of $D^{melt/cpx}_{M}$ with $^{iv}Al^{cpx}$ or CaO to Mo (and W), showing that Mo is not a good proxy for the HFSEs in this instance.

5.3. Two-element distribution coefficients

For most applications of partition coefficients to petrological problems, the variation of activity coefficients with melt composition is a nuisance that obscures the information being sought. One way to minimize the effect of melt composition is to use two-element distribution coefficients. For an element

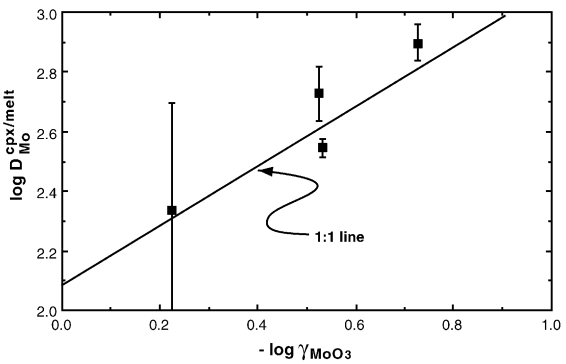

Fig. 12. Correlation between observed partition coefficient for Mo between clinopyroxene and melt from the experiments of Hill et al. (2000), and values of $\gamma^{sil\ melt}_{MoO_3}$ calculated from the results of this study. The slope is unity within error (shown as the 1:1 line): all the variation in $D^{melt/cpx}_{Mo}$ is accounted for by the effect of melt composition.

M_A, the generalized melt/crystal partitioning reaction is:

$$M_AO_{x/2} \cdot \underset{\substack{Z\\ \text{crystal}}}{\sum} n\ ZO_{y/2} = M_AO_{x/2}\ (\text{melt}) + \sum_Z n\ ZO_{y/2}\ (\text{melt}) \quad (24)$$

hence

$$\ln D_{M_A}^{\text{melt/crystal}} = -\Delta_m G^o(M_A)/RT - \sum_Z n \ln a_{ZO_{y/2}}^{\text{melt}} - \ln \gamma_{M_AO_{x/2}}^{\text{melt}} + \ln \gamma_{M_AO\cdot\sum_Z n\ ZO_{y/2}}^{\text{crystal}} + \ln k \quad (25)$$

If an element M_B of the same valence and with similar crystal-chemical properties such as ionic radius can be identified, then a corresponding reaction can be written for this element. Subtraction of the two reactions eliminates the effect of the "structural components" (i.e., the $\sum_Z n \cdot \ln a_{ZO_{y/2}}$ terms) and also the term in ln k, leaving a rather simple expression for the two-element distribution coefficient, $Kd_{M_A-M_B}^{\text{crystal/melt}}$:

$$\ln Kd_{M_A-M_B}^{\text{crystal/melt}} = \ln\left(D_{M_A}^{\text{melt/crystal}} \Big/ D_{M_B}^{\text{melt/crystal}}\right) = -\Delta_r G^o(M_A - M_B)/RT - \ln\left(\gamma_{M_AO_{x/2}}^{\text{melt}} \Big/ \gamma_{M_BO_{x/2}}^{\text{melt}}\right) + ln\left(\gamma_{M_AO\cdot\sum_Z n\ ZO_{y/2}}^{\text{crystal}} \Big/ \gamma_{M_BO\cdot\sum_Z n\ ZO_{y/2}}^{\text{crystal}}\right) \quad (26)$$

where $\Delta_r G^o$ (M_A–M_B) is the free energy of the exchange reaction:

$$M_AO_{x/2}\ (\text{melt}) + M_BO_{x/2}\ (\text{crystal}) \cdot \sum_Z n\ ZO_{y/2} = M_BO_{x/2}\ (\text{melt}) + M_AO_{x/2}\ (\text{crystal}) \cdot \sum_Z n\ ZO_{y/2} \quad (27)$$

Most of the effect of melt composition also drops out of ratios taken between any two of $\gamma_{FeO}^{\text{sil melt}}$, $\gamma_{NiO}^{\text{sil melt}}$, and $\gamma_{CoO}^{\text{sil melt}}$, as implied by the good positive correlations shown in Fig. 6a,b. This is illustrated in Fig. 12a,b. Thus, two-element distribution coefficients, as well as eliminating the effect of melt composition due to the structural components (the "stoichiometric control"), may also greatly reduce the other effect of melt composition on trace-element partition coefficients, that coming from the activity coefficients. The efficacy of the two-element approach in the former context has long been appreciated (e.g., Takahashi and Irvine, 1981); but its almost equal usefulness as regards the activity coefficients has gone unappreciated since so little was known about activity coefficients of trace elements in silicate melts anyway.

The ratios $\gamma_{FeO}^{\text{sil melt}}/\gamma_{NiO}^{\text{sil melt}}$ and $\gamma_{CoO}^{\text{sil melt}}/\gamma_{NiO}^{\text{sil melt}}$, like $\gamma_{MoO_2}^{\text{sil melt}}/\gamma_{MoO_3}^{\text{sil melt}}$, are not completely constant, but whereas the latter depends on X_{CaO}, $\gamma_{FeO}^{\text{sil melt}}/\gamma_{NiO}^{\text{sil melt}}$ and $\gamma_{CoO}^{\text{sil melt}}/\gamma_{NiO}^{\text{sil melt}}$ depend on X_{SiO_2}, albeit but slightly, as shown in Fig. 13a,b. The variation in $\gamma_{NiO}^{\text{sil melt}}/\gamma_{FeO}^{\text{sil melt}}$ is not inconsistent with the correlation between $\gamma_{FeO}^{\text{sil melt}}$ and $\gamma_{NiO}^{\text{sil melt}}$, shown in Fig. 6a, since the slope of the correlation is not unity; the two-element distribution coefficient does not quite eliminate all the effects of melt composition. A similar subtle variation of $\gamma_{MgO}^{\text{sil melt}}/\gamma_{FeO}^{\text{sil melt}}$ with X_{SiO_2} can also be observed in the experimental data on $Kd_{Fe-Mg}^{\text{ol/melt}}$, the Fe^{2+}–Mg distribution between olivine and melt (O'Neill, unpublished data). The ratio $\gamma_{CoO}^{\text{sil melt}}/\gamma_{FeO}^{\text{sil melt}}$ also shows a correlation with X_{SiO_2}, but with the datum for the CAS3 composition as a significant anomaly.

Two-element distribution coefficients have been used explicitly, for example, when dealing with the partitioning of Fe^{2+} and Mg between olivine and melt (e.g., Roeder and Emslie, 1970). However, the two-element approach is often used implicitly in the way that trace-element data are interpreted. This happens when the shape of an REE pattern is considered, rather than the absolute abundance of a particular REE. Effectively, this normalizes the REE to one value, and the effects of melt composition, which should be similar for all REEs, cancel. Thus, the shape of an REE pattern should be largely independent of melt composition, whereas absolute abundances will reflect the influence on $D_{REE}^{\text{melt/crystal}}$ of the activities of the structural components as well as $\gamma_{REE_2O_3}^{\text{melt}}$. Almost nothing is yet known about the latter. This means that although the shape of REE patterns should provide robust evidence on the identities of crystalline phases in the

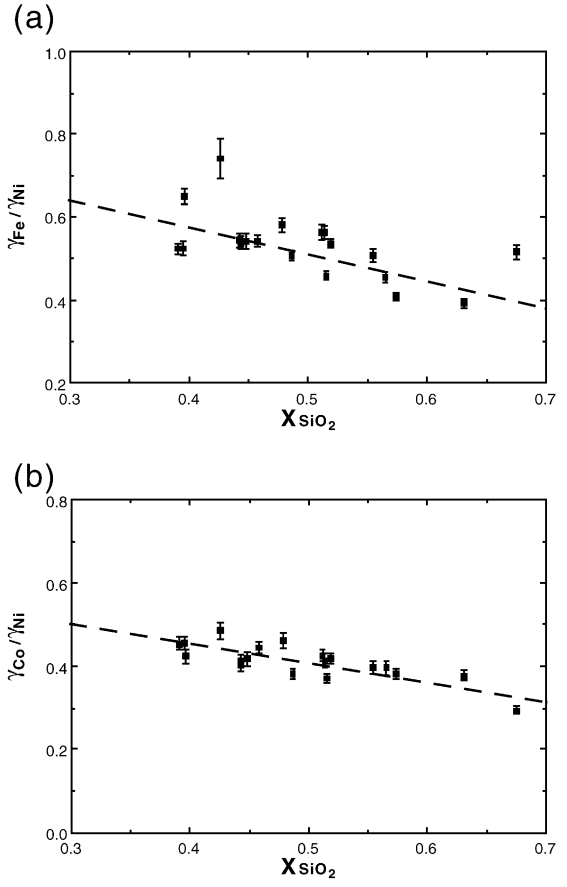

Fig. 13. The ratios (a) $\gamma_{FeO}^{sil\ melt}/\gamma_{NiO}^{sil\ melt}$, and (b) $\gamma_{CoO}^{sil\ melt}/\gamma_{NiO}^{sil\ melt}$ as a function of X_{SiO_2}. The dashed lines are least-squares best fits.

residue during partial melting, some skepticism should be attached to the more quantitative pretensions of REE inversion modelling.

Similar observations can be made about Onuma diagrams. In these diagrams, values of $D_M^{melt/crystal}$ for a series of elements with the same valence are plotted as a function of their ionic radius. The plots generally form a parabola. This maximum on the parabola is interpreted as being the optimum ionic radius for substitution into the crystal structure, with values of $D_M^{melt/crystal}$ decreasing away from this maximum as the ionic radii become less favourable. This implies that, for a series of isovalent elements M, the free energy of the partitioning reaction $\Delta_r G^o$ (M), and the activity coefficient of M in the crystal under consideration, $\gamma_{MO_{x/2}\cdot\sum_Z nZO_{y/2}}^{crystal}$, are both simple smooth functions of the ionic radii of M. For REEs, partition coefficients generally do plot against ionic radii on parabolas in Onuma diagrams, in good agreement with the simple theory (Brice, 1975; Wood and Blundy, 1997). However, this does not imply that the contribution to the partition coefficients from the melt composition is negligible (i.e., that the melt behaves as an ideal solution), as the effect of melt composition should be similar for all the REE.

The results of this study show that individual activity coefficients for trace-element oxide components in silicate melts are complex functions of the major-element composition of the melt, and cannot at present be predicted accurately. However, the ratio of activity coefficients for two oxide components of geochemically similar elements seems to behave much more simply, and in the two groups investigated here (i.e., MoO_2–MoO_3 on one hand and FeO–NiO–CoO on the other), these ratios are simple functions of one major-element component. This raises the question of how these insights might be generalized to other trace elements.

5.4. Complexes in silicate melts and activity coefficients

Silicate melts are structurally complicated, but are often modelled thermodynamically as consisting of molecular units with the stoichiometry of common liquidus phases (Burnham, 1981; Mysen, 1990; Ghiorso and Sack, 1995). Given this tradition, it seems reasonable to ascribe the decrease of $\gamma_{MoO_2}^{sil\ melt}$ and $\gamma_{MoO_3}^{sil\ melt}$ with X_{CaO} and to a lesser extent X_{MgO} to the role of molecular units or complexes of the type $CaMo^{6+}O_4$, $CaMo^{4+}O_3$, $MgMo^{6+}O_4$ and $MgMo^{4+}O_3$. We have not been able to discover any information about ternary phases in the system SiO_2–Mo–O in the literature, suggesting that Mo–silicate phases are not stable, and, therefore, that Mo–silicate complexes would not be important.

To explore this idea more quantitatively, we have plotted in Fig. 14 the W parameters from our fitting of $\gamma_{MoO_2}^{sil\ melt}$ and $\gamma_{MoO_3}^{sil\ melt}$ (Table 8 and Eqs. (14)–(16)) against the free energies of formation from the oxides of the crystalline compounds of the same stoichiom-

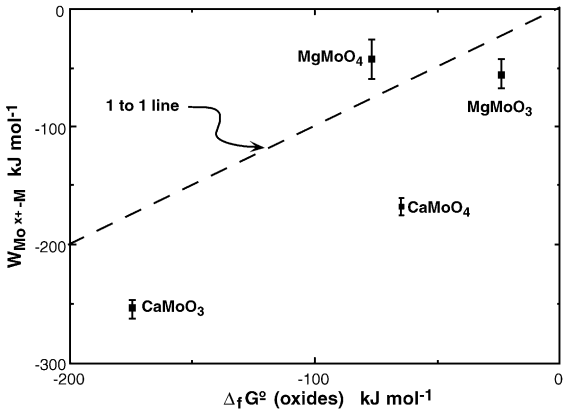

Fig. 14. Inferred interaction parameters (W parameters) for Mo^{x+}–Ca and Mo^{x+}–Mg interactions (from Table 8) versus the free energy of formation from the oxides at 1400 °C of the solids with the same stoichiometry.

etry as the hypothetical complexes (data from Kubaschewski, 1972). In assessing Fig 14, it needs to be remembered that the free energy data are not always well known and in some cases are little more than guesses (e.g., for $MgMoO_3$). Also, the free energies of formation of ternary oxides are the sum of many types of chemical energies including the purely geometrical contributions imposed by the crystal structure, which would not be expected to be reflected in the energies of formation of the hypothetical melt complexes.

Nevertheless, there is indeed the hint of a correlation, and the magnitude of the W parameters is similar to the free energies of formation. Obviously, more data are needed, but in the interim, this approach looks more promising than one based simply on an electronegativity scale, and may be used to make some general predictions about trace element activity coefficients in silicate melts.

Other HFSE oxides such as ZrO_2, HfO_2, Nb_2O_5, and Ta_2O_5, also form stable ternary oxide compounds with CaO with large negative free energies of formation (e.g., Kubaschewski, 1972; Barin et al., 1989; Levin et al., 1964), and their activity coefficients in silicate melts may be expected to show a similar sensitivity to the CaO-content of the melt as $\gamma^{\text{sil melt}}_{MoO_2}$ and $\gamma^{\text{sil melt}}_{MoO_3}$. However, ZrO_2 and HfO_2, unlike Nb_2O_5, and Ta_2O_5, do not form stable compounds with MgO, leading to a prediction that the behaviour of Zr and Hf may be less sensitive than Nb and Ta to the MgO content of the melt. UO_2 and ThO_2 do not form particularly stable compounds with CaO or MgO and their activity coefficients may therefore be expected to also be less sensitive to melt composition. UO_3 does form a stable ternary oxide with CaO, which may be important in stabilizing U^{6+} over U^{4+}. The oxidation state of U in magmas may have implications for the fractionation of U from Th.

In general, the oxides of less electronegative elements form even more stable ternary compounds with HFSE oxides, the geologically important example being Na_2O. For example, the free energy of formation of Na_2MoO_4 from the oxides is over twice that of $CaMoO_4$ at the same temperature, leading to an expectation that Na_2O in silicate melts would greatly lower $\gamma^{\text{sil melt}}_{MoO_3}$. The relative effect on $\gamma^{\text{sil melt}}_{MoO_2}$ cannot be predicted, as we could find no data for Na_2MoO_3. Quantification of the effect of Na_2O on $\gamma^{\text{sil melt}}_{MoO_2}$ and $\gamma^{\text{sil melt}}_{MoO_3}$ is a point of some importance not addressed in this study because of the experimental difficulties associated with Na volatilization.

The Rare Earth Element oxides REE_2O_3 do not form stable ternary compounds with CaO or MgO (Levin et al., 1964) and probably not with Na_2O (no information on Na_2O–REE_2O_3 compounds was found in the literature, circumstantial evidence that they are not particularly stable). This implies that REE activity coefficients ($\gamma^{\text{melt}}_{REE_2O_3}$) would be much less sensitive to melt composition than HFSE activity coefficients. On the other hand, the REEs do form very stable perovskite and garnet phases with Al_2O_3 ($REEAlO_3$ and $REE_3Al_5O_{12}$; also with other trivalent oxides such as Fe_2O_3), which may indicate $\gamma^{\text{melt}}_{REE_2O_3}$ in silicate melts might depend on Al_2O_3. Theoretical modelling of this possibility by Van Westrenen et al. (2000) has indicated otherwise, and it may be that the great stability of the REE_2O_3–Al_2O_3 ternary oxides is simply due to the particularly favorable geometry of the perovskite and garnet structures. As pointed out earlier, there are as yet no measurements of the activities of REEs in silicate melts to test this supposition directly.

Of course, REE crystal/melt partition coefficients must also depend on melt composition through the effects of the activities of the structural components associated with the way the REE substitutes into the crystal (the stoichiometry constraint). This is likely to confound any attempt to extract activity coefficients from crystal/melt partition coefficients directly.

5.5. Universal melt descriptors

A recurrent theme in the study of silicate melts in the fields of both metallurgy and the earth sciences has been the search for a single parameter by which the major properties of the silicate melt can be described. Examples are "optical basicity" (see, e.g., Duffy, 1993) or the parameter known as NBO/T, meaning the (somewhat hypothetical) ratio of nonbridging oxygens to tetrahedrally coordinated cations (e.g., Mysen et al., 1985; Mysen, 1990). For example, the sulfide capacity of a silicate melt (a measure of the ability of the melt to dissolve sulfide) has often been related to optical basicity (e.g., Young et al., 1992), albeit with dubious effectiveness (Mavrogenes and O'Neill, 1999).

Righter and Drake (1997) have used the NBO/T parameter to characterize the effect of melt composition on siderophile-element partition coefficients. The present experimental data are ideally suited to test this approach. Values of NBO/T are given in Table 1. We have not assigned a value to the $AD + TiO_2$ composition because of the uncertain status of TiO_2 in determining NBO/T. In Fig. 15a, values of $\gamma_{MoO_3}^{sil\ melt}$ are plotted against NBO/T. There appears to be some correlation, $\gamma_{MoO_3}^{sil\ melt}$ decreasing with increasing NBO/T, but the correlation is inferior to that obtained between $\gamma_{MoO_3}^{sil\ melt}$ and the simple compositional parameter X_{CaO}, shown in Fig. 5b. The correlation may even be mostly an artefact, caused by the limitations on melt composition that our chosen experimental temperature of 1400 °C imposes, since MgO-rich compositions with high NBO/T are below their liquidus. For both $\gamma_{MoO_2}^{sil\ melt}$ and $\gamma_{MoO_3}^{sil\ melt}$, our experiments establish that there is a large difference between MgO and CaO in determining $\gamma_{MoO_2}^{sil\ melt}$ and $\gamma_{MoO_3}^{sil\ melt}$, whereas the NBO/T parameter does not distinguish between the effects of MgO and CaO.

For the FeO, NiO and CoO data, the results are even more clear-cut in showing that NBO/T is an inadequate parameter for describing activity coefficients (e.g., Fig. 15b). The correlation coefficient for a regression between $\gamma_{NiO}^{sil\ melt}$ and NBO/T is zero to three decimal places.

These conclusions may appear contrary to some previous results. For example, for Ni, Mysen and Virgo (1980) presented an excellent linear correlation between experimentally measured values of the partition coefficient of Ni between olivine and silicate melt ($D_{Ni}^{ol/melt}$), and NBO/T. However, because of the stoichiometric constraint, $D_{Ni}^{ol/melt}$ depends on $a_{SiO_2}^{melt}$, which is a strong function of NBO/T in the binary join across the system $NaAlSi_3O_8$–$CaAl_2Si_2O_6$–Mg_2SiO_4 used by Mysen and Virgo. Their results do not really address the question of how $\gamma_{NiO}^{sil\ melt}$ may vary. A similar comment applies to the correlations shown by Kohn and Schofield (1994) for the distribution of Mn and Zn between olivine and melt in the same system, although here, the interpretation of the results is further complicated by variation in temperature.

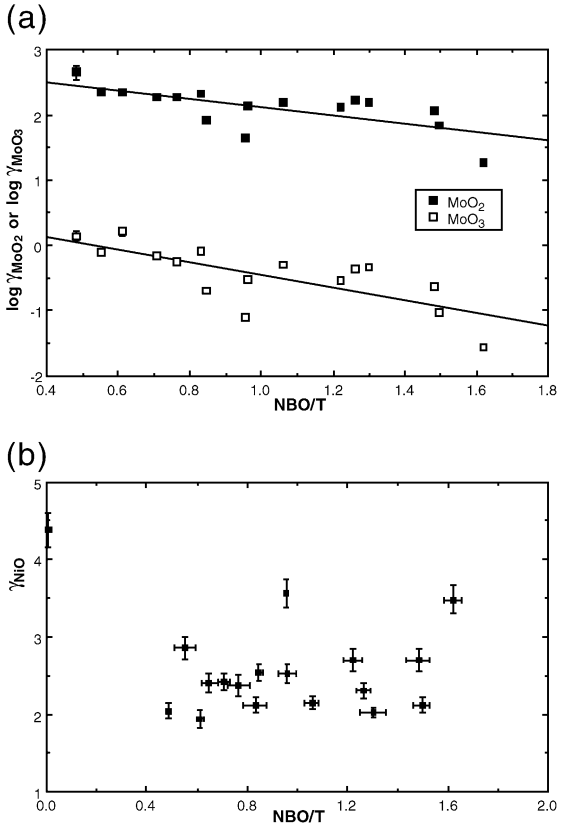

Fig. 15. (a) log $\gamma_{MoO_2}^{sil\ melt}$ and log $\gamma_{MoO_3}^{sil\ melt}$; (b) $\gamma_{NiO}^{sil\ melt}$ versus NBO/T, the number of nonbridging oxygens to tetrahedral cations in the melt. Error bars are two standard deviations, and are not shown in (a) for clarity. While there appears to be a good correlation between both log $\gamma_{MoO_2}^{sil\ melt}$ and log $\gamma_{MoO_3}^{sil\ melt}$ and NBO/T, comparison with Fig. 5a,b shows that a better correlation is found between log $\gamma_{MoO_2}^{sil\ melt}$ and log $\gamma_{MoO_3}^{sil\ melt}$ and X_{CaO}. For $\gamma_{NiO}^{sil\ melt}$, there is no correlation with NBO/T at all.

Recently, Jaeger and Drake (2000) have measured activity coefficients of Co, W (presumably similar in behaviour to Mo^{4+}) and Ga in a series of silicate melt compositions in the system CMAS–TiO_2 and presented the results as functions of NBO/T. Whereas $\gamma_{CoO}^{sil\ melt}$ does not vary with composition, the activity coefficients for WO_2 were claimed to show an excellent correlation with NBO/T. However, the melt compositions used by Jaeger and Drake are linear combinations obtained by mixing different proportions of just two end-member compositions. The apparent correlation with NBO/T is an artefact of this.

Any general correlation between activity coefficients and NBO/T would seem to be ruled out by some basic definitions. Raoult's law requires always that $\gamma_{MO_{x/2}}^{sil\ melt} \rightarrow 1$ as $X_{MO_{x/2}} \rightarrow 1$ regardless of the value of $\gamma_{MO_{x/2}}^{sil\ melt}$ at infinite dilution ($X_{MO_{x/2}} \rightarrow 0$). However, NBO/T must change by different rules, depending on whether $MO_{x/2}$ is regarded as a network former or modifier. This is demonstrated by the results of Doyle and Naldrett (1986) and Doyle (1988, 1989) on $\gamma_{FeO}^{sil\ melt}$. The value of NBO/T for a pure FeO melt is infinity; hence, $\gamma_{FeO}^{sil\ melt} \rightarrow 1$ as NBO/T $\rightarrow \infty$ with increasing X_{FeO}. Yet, the slope of this trend can be either positive or negative, depending on whether the value of $\gamma_{FeO}^{sil\ melt}$ at infinite dilution is less than or greater than 1. The same sort of argument can be made for trying to relate activity coefficients to optical basicity.

In conclusion, we suggest that attempts to relate activity coefficients and hence trace-element partition coefficients to universal melt descriptors are misguided and doomed to failure.

Acknowledgements

We thank Astrid Holzheid and Jon Blundy for helpful reviews, especially the latter for pointing out the Hill et al. (2000) results, and Roberta Rudnick for her editorial handling. **[RR]**

References

Banno, S., Matsui, Y., 1973. On the formulation of partition coefficients for trace elements distribution between minerals and magma. Chem. Geol. 11, 1–15.

Barin, I., Sauert, F., Schultze-Rhonhof, E., Sheng, W.S., 1989. Thermochemical Data of Pure Substances, Part I and Part II. VCH Verlagsgesellschaft, Weinheim, Germany, pp. 1–1739.

Blundy, J.D., Wood, B.J., 1991. Crystal-chemical controls on the partitioning of Sr and Ba between plagioclase feldspar, silicate melts and hydrothermal solutions. Geochim. Cosmochim. Acta 55, 193–209.

Blundy, J.D., Wood, B.J., 1994. Prediction of crystal-melt partition coefficients from elastic moduli. Nature 372, 452–454.

Brice, J.C., 1975. Some thermodynamic aspects of the growth of strained crystals. J. Cryst. Growth 28, 249–253.

Burnham, C.W., 1981. The nature of multicomponent aluminosilicate melts. Phys. Chem. Earth 13, 197–229.

Campbell, I.H., Naldrett, A.J., Roeder, P.L., 1979. Nickel activity in silicate liquids: some preliminary results. Can. Mineral. 17, 495–505.

Chase, M.W., 1998. NIST-JANAF thermochemical tables. J. Phys. Chem. Ref. Data. American Chemical Society, Washington, DC, USA. Part 1: 1–958, Part 2: 959–1952.

Davies, P.K., Navrotsky, A., 1983. Quantitative correlations of deviations from ideality in binary and pseudo-binary solid solutions. J. Solid State Chem. 46, 1–22.

DePaolo, D.J., 1981. Trace-element and isotopic effects of combined wallrock assimilation and fractional crystallization. Earth Planet. Sci. Lett. 53, 189–202.

Dingwell, D.B., Ertel, W., O'Neill, H.S.C., Spettel, B., 1994. The solubility and oxidation state of nickel in silicate melt at low oxygen fugacities: results using a mechanically assisted equilibrium technique. Geochim. Cosmochim. Acta 58, 1967–1974.

Doyle, C.D., 1988. Prediction of the activity of FeO in multicomponent magma from known values in [SiO_2–$KAlO_2$–$CaAl_2Si_2O_8$]–FeO liquids. Geochim. Cosmochim. Acta 52, 1827–1834.

Doyle, C.D., 1989. The effect of substitution of TiO_2 for SiO_2 on a_{FeO} in magma. Geochim. Cosmochim. Acta 53, 2631–2638.

Doyle, C.D., Naldrett, A.J., 1986. Ideal mixing of divalent cations in mafic magma and its effect on the solution of ferrous oxide. Geochim. Cosmochim. Acta 50, 435–443.

Doyle, C.D., Naldrett, A.J., 1987. Ideal mixing of divalent cations in mafic magma: II. The solution of NiO and the partitioning of nickel between coexisting olivine and liquid. Geochim. Cosmochim. Acta 51, 213–219.

Dudson, P.J., Fraser, D.G., 1981. Nickel oxide activities in silicate melts in the system CaO–MgO–Al_2O3–SiO_2–NiO, Progress in Experimental Petrology, The Natural Environmental Research Council Publications Series D 18, 247–251.

Duffy, J.A., 1993. A review of optical basicity and its applications to oxidic systems. Geochim. Cosmochim. Acta 57, 3961–3970.

Eggins, S.M., Woodhead, J.D., Kinsley, L.P.J., 1997. A simple method for the precise determination of >=40 trace elements in geological samples by ICPMS using enriched isotope internal standardisation. Chem. Geol. 134 (4), 311–326.

Eggins, S.M., Rudnick, R.L., McDonough, W.F., 1998. The composition of peridotites and their minerals: a laser-ablation ICP-MS study. Earth Planet. Sci. Lett. 154 (1–4), 53–71.

Ertel, W., O'Neill, H.S.C., Dingwell, D.B., Spettel, B., 1996. Solubility of tungsten in a haplobasaltic melt as a function of tem-

perature and oxygen fugacity. Geochim. Cosmochim. Acta 60 (7), 1171–1180.

Ertel, W., Dingwell, D.B., O'Neill, H.S.C., 1997. Compositional dependence of the activity of nickel in silicate melts. Geochim. Cosmochim. Acta 61 (22), 4707–4721.

Ertel, W., O'Neill, H.S.C., Sylvester, P.J., Dingwell, D.B., 1999. Solubilities of Pt and Rh in a haplobasaltic silicate melt at 1300 °C. Geochim. Cosmochim. Acta 63 (16), 2439–2449.

Ertel, W., O'Neill, H.S.C., Sylvester, P.J., Dingwell, D.B., Spettel, B., 2001. The solubility of rhenium in silicate melts: implications for the geochemical properties of rhenium at high temperatures. Geochim. Cosmochim. Acta 65, 2161–2170.

Fitton, J.G., 1995. Coupled molybdenum and niobium depletion in continental basalts. Earth Planet. Sci. Lett. 136, 715–721.

Gast, P.W., 1968. Trace element fractionation and the origin of tholeiitic and alkaline magma types. Geochim. Cosmochim. Acta 32, 1057–1086.

Ghiorso, M.S., Sack, R.O., 1995. Chemical mass transfer in magmatic processes IV. A revised and internally consistent thermodynamic model for the interpolation and extrapolation of liquid–solid equilibria in magmatic systems at elevated temperatures and pressures. Contrib. Mineral. Petrol. 119, 197–212.

Grimsey, E.J., Biswas, A.K., 1976. Solubility of nickel in silica-saturated iron silicate slags at 1573 K. Inst. Min. Metall., Trans. C 85, 200–207.

Grimsey, E.J., Biswas, A.K., 1977. Solubility of nickel in iron-silicate slags both lime-free and with lime at 1573 K. Inst. Min. Metall., Trans., Sect. C 86, 1–8.

Helffrich, G., Wood, B., 1989. Subregular model for multicomponent solutions. Am. Mineral. 74, 1016–1022.

Hill, E., Wood, B.J., Blundy, J.D., 2000. The effect of Ca-Tschermaks component on trace element partitioning between clinopyroxene and silicate melt. Lithos 53, 203–215.

Holzheid, A., Palme, H., 1996. The influence of FeO on the solubility of Co and Ni in silicate melts. Geochim. Cosmochim. Acta 60, 1181–1193.

Holzheid, A., Borisov, A., Palme, H., 1994. The effect of oxygen fugacity and temperature on solubilities of nickel, cobalt, and molybdenum in silicate melts. Geochim. Cosmochim. Acta 58 (8), 1975–1981.

Holzheid, A., Palme, H., Chakraborty, S., 1997. The activities of NiO, CoO and FeO in silicate melts. Chem. Geol. 139, 21–38.

Jaeger, W.L., Drake, M.J., 2000. Metal–silicate partitioning of Co, Ga, and W: dependence on silicate melt composition. Geochim. Cosmochim. Acta 64 (22), 3887–3895.

Kohn, S.C., Schofield, P.F., 1994. The importance of melt composition in controlling trace-element behaviour: an experimental study of Mn and Zn partitioning between forsterite and silicate melts. Chem. Geol. 117, 73–87.

Kubaschewski, O., 1972. The thermodynamic properties of double oxides (a review). High Temp. High Pressure 4, 1–12.

Lacy, A.M., Pask, J.A., 1970. Electrochemical studies in glass: I. The system $NiO–Na_2Si_2O_5$. J. Am. Ceram. Soc. 53 (10), 559–562.

Levin, E.M., Robbins, C.R., McMurdie, H.F., 1964. Phase diagrams for ceramists. Am. Ceram. Soc., 1–601.

Liu, S.-H., Fruehan, R.J., Morales, A., Ozturk, B., 2001. Measurement of FeO activity and solubility of MgO in smelting slags. Metall. Mater., Trans. B 32B, 31–36.

Longerich, H.P., Jackson, S.E., Gunther, D., 1996. Laser ablation inductively coupled plasma mass spectrometric transient signal data acquisition and analyte concentration calculation. J. Anal. At. Spectrom. 11 (9), 899–904.

Longhi, J., 1987. Liquidus equilibria and solid solution in the system $CaAl_2Si_2O_8–Mg_2SiO_4–CaSiO_3–SiO_2$ at low pressure. Am. J. Sci. 287, 265–331.

Mavrogenes, J.A., O'Neill, H.S.C., 1999. The relative effects of pressure, temperature and oxygen fugacity on the solubility of sulfide in mafic magmas. Geochim. Cosmochim. Acta 63, 1173–1180.

McKenzie, D., O'Nions, R.K., 1991. Partial melt distributions from inversion of REE concentrations. J. Petrol. 32, 1021–1091.

Mysen, B.O., 1990. Relationships between silicate melt structure and petrologic processes. Earth-Sci. Rev. 27, 281–365.

Mysen, B.O., Virgo, D., 1980. Trace element partitioning and melt structure: an experimental study at 1 atm pressure. Geochim. Cosmochim. Acta 44, 1917–1930.

Mysen, B.O., Virgo, D., Seifert, F., 1985. Relationships between properties and structure of aluminosilicate melts. Am. Mineral. 70, 88–105.

Navon, O., Stolper, E.M., 1987. Geochemical consequences of melt percolation: the upper mantle as a chromatographic column. J. Geol. 95, 285–307.

Nielsen, R.L., 1988. A model for the simulation of the combined major and trace element liquid lines of descent. Geochim. Cosmochim. Acta 52, 27–38.

O'Hara, M.J., 1995. Trace element geochemical effects of integrated melt extraction and 'shaped' melting regimes. J. Petrol. 36, 1111–1132.

O'Neill, H.S.C., 1986. The $Mo–MoO_2$ (MOM) oxygen buffer and the free energy of formation of MoO_2. Am. Mineral. 71, 1007–1010.

O'Neill, H.S.C., Palme, H., 1998. Composition of the silicate earth: implications for accretion and core formation. In: Jackson, I. (Ed.), The Earth's Mantle—Composition, Structure and Evolution. Cambridge Univ. Press, Cambridge, UK, pp. 3–126.

O'Neill, H.S.C., Pownceby, M.I., 1993. Thermodynamic data from redox reactions at high temperatures: I. An experimental and theoretical assessment of the electrochemical method using stabilized zirconia electrolytes, with revised values for the Fe–"FeO", Co–CoO, Ni–NiO and $Cu–Cu_2O$ oxygen buffers, and new data for the $W–WO_2$ buffer. Contrib. Mineral. Petrol. 114, 296–314.

Pearce, N.J.G., Perkins, W.T., Westgate, J.A., Gordon, M.P., Jackson, S.E., Neal, C.R., Chenery, S.P., 1997. A compilation of new and published major and trace element data for NIST SRM 610 and NIST SRM 612 glass reference materials. Geostand. Newsl. J. Geostand. Geoanal. 21 (1), 115–144.

Pretorius, E.B., Muan, A., 1992. Activity of nickel(II) oxide in silicate melts. J. Am. Ceram. Soc. 75 (6), 1490–1496.

Richardson, C., McKenzie, D., 1994. Radioactive disequilibria from 2D models of melt generation by plumes and ridges. Earth Planet. Sci. Lett. 128, 425–437.

Righter, K., Drake, M.J., 1997. Metal–silicate equilibrium in a

homogeneously accreting earth: new results for Re. Earth Planet. Sci. Lett. 146, 541–553.

Roeder, P.L., 1974. Activity of iron and olivine solubility in basaltic liquids. Earth Planet. Sci. Lett. 23, 397–410.

Roeder, P.L., Emslie, R.F., 1970. Olivine–liquid equilibrium. Contrib. Mineral. Petrol. 29, 275–289.

Shaw, D.M., 2000. Continuous (dynamic) melting theory revisited. Can. Mineral. 38, 1041–1063.

Snyder, D.A., Carmichael, I.S.E., 1992. Olivine–liquid equilibria and the chemical activities of FeO, NiO, Fe_2O_3, and MgO in natural basic melts. Geochim. Cosmochim. Acta 56, 303–318.

Spiegelman, M., Elliott, T., 1993. Consequences of melt transport for uranium series disequilibrium in young lavas. Earth Planet. Sci. Lett. 118, 1–20.

Sylvester, P.J., Eggins, S.M., 1997. Analysis of Re, Au, Pd, Pt and Rh in NIST glass certified reference materials and natural basalt glasses by laser ablation ICP-MS. Geostand. Newsl. 21, 215–229.

Takahashi, E., Irvine, T.N., 1981. Stoichiometric control of crystal/liquid single-component partition coefficients. Geochim. Cosmochim. Acta 45, 1181–1185.

Van Westrenen, W., Blundt, J.D., Wood, B.J., 2000. Atomistic simulation of trace element incorporation into garnets—comparison with experimental garnet-melt partitioning data. Geochim. Cosmochim. Acta 64, 1629–1639.

Walter, M.J., Thibault, Y., 1995. Partitioning of tungsten and molybdenum between metallic liquid and silicate melt. Science 270, 1186–1189.

Ware, N.G., 1981. Computer programs and calibration with the PIBS technique for quantitative electron probe analysis using a lithium-drifted silicon detector. Comput. Geosci. 7, 167–184.

Wood, B.J., Blundy, J.D., 1997. A predictive model for rare earth element partitioning between clinopyroxene and anhydrous silicate melt. Contrib. Mineral. Petrol. 129, 166–181.

Wood, B.J., Fraser, D.G., 1977. Elementary Thermodynamics for Geologists. Oxford Univ. Press, Oxford, UK.

Young, R.W., Duffy, J.A., Hassall, G.J., Xu, Z., 1992. Use of optical basicity concept for determining phosphorus and sulphur slag-metal partitions. Ironmaking Steelmaking 19, 201–219.